JOURNAL OF GEOPHYSICAL RESEARCH, VOL. 110, B03403, doi:10.1029/2004JB003209, 2005

Block models of crustal motion in southern California constrained by GPS measurements

Brendan J. Meade[1] and Bradford H. Hager

Department of Earth, Atmospheric and Planetary Sciences, Massachusetts Institute of Technology, Cambridge, Massachusetts, USA

Received 3 June 2004; revised 19 December 2004; accepted 3 January 2005; published 16 March 2005.

[1] We estimate slip rates on major active faults in southern California using a block model constrained by Global Positioning System measurements of interseismic deformation. The block model includes the effects of block rotation and elastic strain accumulation consistent with a simple model of the earthquake cycle. Our estimates of the right-lateral strike-slip rate on the San Andreas fault vary by at least a factor of 5, from a high of 35.9 ± 0.5 mm/yr in the Carrizo Plain to a low of 5.1 ± 1.5 mm/yr through the San Bernadino segment. Shortening across the Puente Hills Thrust and left-lateral slip on the Raymond Hill fault are consistent with both thickening and escape tectonics in the Los Angeles Basin. Discrepancies between geodetic and geologic slip rate estimates along the San Andreas and San Jacinto faults, as well as in the Eastern California Shear Zone, may be explained by a temporal change in fault system behavior. We find no substantial evidence for long-term postseismic relaxation and infer that the viscosity of the lower crust/upper mantle may be relatively high ($\eta > 10^{19}$ Pa s).

Citation: Meade, B. J., and B. H. Hager (2005), Block models of crustal motion in southern California constrained by GPS measurements, *J. Geophys. Res.*, *110*, B03403, doi:10.1029/2004JB003209.

1. Introduction

[2] The southern California fault system (SCFS) lies at the boundary between the Pacific and North American Plates. At the latitude of the Carrizo plain, approximately 70% of the total relative plate motion (~50 mm/yr) [e.g., *DeMets et al.*, 1990; *DeMets and Dixon*, 1999] is localized as right-lateral slip on the San Andreas fault (SAF) [e.g., *Sieh and Jahns*, 1984; *Minster and Jordan*, 1987; *Argus and Gordon*, 2001]. Other subparallel structures, including the San Jacinto fault (SJF) and the Eastern California Shear Zone (ECSZ), intersect with the SAF and accommodate 10–15 mm/yr of right-lateral motion [e.g., *Sharp*, 1981; *Sauber et al.*, 1994; *McClusky et al.*, 2001; *Savage et al.*, 2001]. Faults that are nearly orthogonal to the relative plate motion vector tend to exhibit left-lateral dip-slip faulting. The geologic record provides evidence for left-lateral motion along the Garlock [e.g., *McGill and Sieh*, 1993; *McGill and Rockwell*, 1998], Pinto Mountain [*Jennings*, 1994; *Petersen and Wesnousky*, 1994], and Raymond Hill faults [*Weaver and Dolan*, 2000]. Southwest of the SAF, the San Gabriel range front and Ventura Basin are defined by active thrust faults.

[3] Earthquake focal mechanisms show a similar variation in orientation and sense of slip (Figure 1). The 1857 Ft. Tejon, 1872 Owens Valley, and 1992 Landers earthquakes are consistent with right-lateral rupture along the SAF and subparallel structures in the ECSZ [e.g., *Ellsworth*, 1990; *Stein and Hanks*, 1998; Y. Y. Kagan, Southern California earthquakes: Extended sources, available at http://scec.ess.ucla.edu/%7eykagan/relm_index.html, University of California, Los Angeles, 2004, hereinafter referred to as Kagan, Southern California Earthquakes: Extended sources, 2004]. Other focal mechanisms from the instrumental era show significant thrust components (e.g., Kern County, 1952, Northridge, 1994) associated with compression across the Big Bend of the SAF and shortening in the Ventura Basin. The earthquake focal mechanisms complement the geologic slip rate data and highlight the diversity of faulting styles in the SCFS.

[4] There has been great interest in determining the distribution of present day deformation in southern California to develop kinematic models of regional tectonics, to constrain the rheology of the lithosphere, and to provide an estimate of where strain is accumulating most rapidly and, thus, where earthquakes will most likely occur. At the regional scale, *Bird and Rosenstock* [1984] developed a hand-fit block model in an effort to combine geologically estimated slip rates in a kinematically consistent manner. *Weldon and Humphreys* [1986] carried out a related study, summing the slip rates from a select group of faults and looking for deviations from a path integral constraint to assess slip rate compatibility. *Minster and Jordan* [1987] quantified the "San Andreas deficit" using an early plate motion model and path integral constraints.

[5] With the development of dense, high precision geodetic networks in the 1970s, it became clear that the effects of interseismic strain accumulation were significant and that

---

[1] Now at Department of Earth and Planetary Sciences, Harvard University, Cambridge, Massachusetts, USA.

0148-0227/05/2004JB003209$09.00

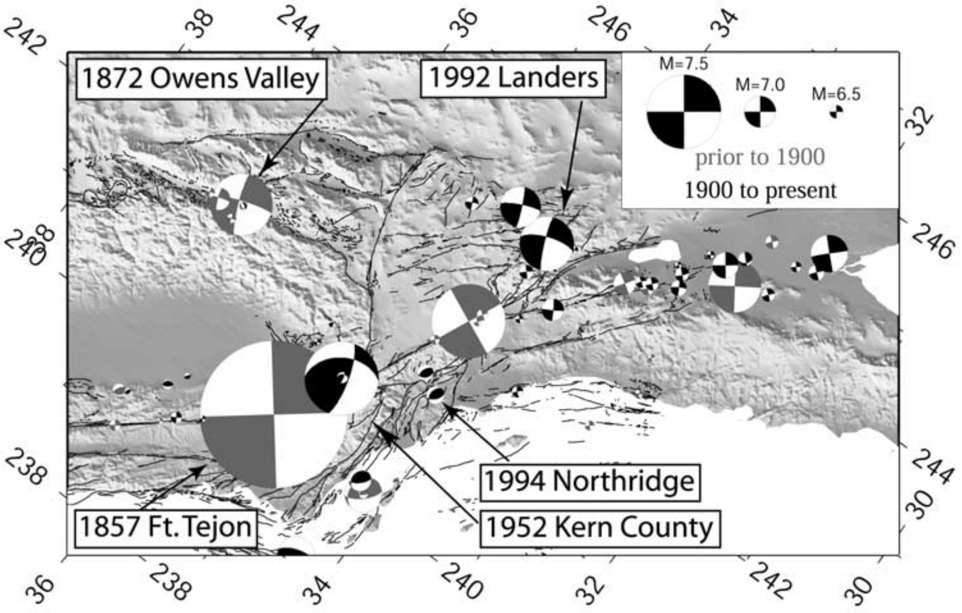

Figure 1. Focal mechanisms for large earthquakes (Kagan, Southern California Earthquakes: Extended sources, 2004) in southern California overlaid on topography (GTOPO30) and fault traces [*Jennings*, 1994]. The area of each focal mechanism is proportional to its scalar seismic moment. The shaded quadrants are compressional. Focal mechanisms with gray compressional quadrants are those from 1807–1900 and those with black compressional quadrants are from 1900–present. The largest focal mechanism is associated with 1857 Ft. Tejon earthquake along the San Andreas fault.

fault slip rates and locking depths could be estimated directly from geodetic data [e.g., *Savage and Burford*, 1973]. Using trilateration data, *Cheng et al.* [1987] developed a block model of the northern Transverse Ranges and found a relatively low slip rate on the SAF. *Saucier and Humphreys* [1993] combined geologic slip rate estimates with VLBI-determined velocities to estimate the horizontal velocity field using a thin elastic sheet finite element model. *Feigl et al.* [1993] used an a priori deep-slip dislocation model that included the San Andreas, San Jacinto, Elsinore, and Garlock faults in an attempt to explain early GPS observations. *Bird and Kong* [1994] updated the block geometry presented by *Bird and Rosenstock* [1984] and developed a model that minimized the difference between strains from a thin elastic sheet finite element model and the strains estimated from EDM and VLBI data. A block model approach was used by *Souter* [1998] to assess the compatibility of geologically determined fault slip rates with each other and with observed GPS velocities. Both *Wdowinski et al.* [2001] and *Smith and Sandwell* [2003] used regional scale geodetic data to model the deformation associated with the SAF. *Becker et al.* [2005] used a block model to estimate fault slip rates and assess the compatibility of interseismic GPS observations and focal mechanism orientations in southern California.

[6] Geodetic data have also been used to resolve slip rates on a more local scale. *Johnson et al.* [1994] and *Bennett et al.* [1996] estimated the strike-slip rate on the southern SAF near the Salton Sea. *Savage and Lisowski* [1998] used a two-dimensional viscoelastic model to estimate not only the slip rate, but also the time within the earthquake cycle, for the Mojave segment of the SAF. The central SAF was studied by *Argus and Gordon* [2001], who attempted to resolve the fault-normal and fault-parallel components of motion. *Segall* [2002] used a Bayesian framework to combine geologic and geodetic data to estimate the slip rate, locking depth, and recurrence intervals for the Carrizo segment of the SAF.

[7] The ECSZ lies to the east of the SAF and accommodates approximately 25% of the relative motion between the Pacific and North American plates. *Sauber et al.* [1986, 1994] and *Savage et al.* [1990] found high strain rates in the southern ECSZ (Mojave Desert), a substantial step toward resolving the San Andreas deficit problem [e.g., *Minster and Jordan*, 1987]. More recently, *Savage et al.* [2001] and *Peltzer et al.* [2001] developed revised estimates of the slip distribution in the Mojave Desert. The ECSZ north of the Garlock fault has also attracted considerable attention, as numerous studies have attempted to estimate the partitioning of slip across the Owens Valley, Panamint Valley, and Death Valley fault zones [e.g., *Bennett et al.*, 1997; *Hearn and Humphreys*, 1998; *Dixon et al.*, 2000; *Gan et al.*, 2000; *McClusky et al.*, 2001; *Miller et al.*, 2001; *Dixon et al.*, 2003].

[8] Geodetic observations of interseismic deformation have also been used to estimate shortening rates in southern California. *Feigl et al.* [1990] estimated the shortening rate across the Santa Maria fold and thrust belt, and *Walls et al.* [1998] carried out a similar study of escape tectonics in the Los Angeles Basin. Neither of these studies accounted for the effects of interseismic strain accumulation. *Donnellan et al.* [1993a, 1993b] and *Hager et al.* [1999] used two-dimensional models to estimate shortening rates and quantify seismic hazard across the Ventura Basin. *Shen et al.* [1996] presented geodetic data for the greater Los Angeles area and the Transverse Ranges. For the Los Angeles Basin,

both *Argus et al.* [1999] and *Bawden et al.* [2001] reached substantially different conclusions than did *Walls et al.* [1998] by including a priori models for the strain accumulation associated with the SAF.

[9] With the availability of regional-scale GPS-determined interseismic velocity fields, we can now model the distribution of deformation across the entire SCFS with great precision. We use a block model approach that establishes a framework for combining geologic and geodetic data into a model that includes the effects of block rotation and interseismic strain accumulation. The block model formulation implicitly enforces a path integral constraint that ensures that the relative plate motion is accommodated everywhere along the length of the plate boundary zone. By estimating slip rates of all faults simultaneously, we arrive at a slip model for southern California that is free of many of the a priori assumptions that have been necessary in previous studies [e.g., *Feigl et al.*, 1993; *Argus et al.*, 1999; *Bawden et al.*, 2001].

2. Relative Deformation Due to Small and Large Earthquakes

[10] During the 5–15 years during which GPS observations have been used to estimate interseismic velocities in southern California, thousands of earthquakes have occurred. The displacements from the $M_W = 7.3$ Landers (1992), $M_W = 6.7$ Northridge (1994), and $M_W = 7.1$ Hector Mine (1999) earthquakes have been studied extensively [e.g., *Hudnut et al.*, 1994, 1996; *Kaverina et al.*, 2002]. Slip models for each of these events have been used to correct GPS time series for the effects of coseismic deformation on interseismic velocity estimates (e.g., Z.-K. Shen et al., The SCEC Crustal Motion Map, Version 3.0, available at http://epicenter.usc.edu/cmm3/, University of Southern California, Los Angeles, 2003, hereinafter referred to as Shen et al., crustal motion map, 2003). However, the displacements and moment release from smaller earthquakes have not been accounted for quantitatively. We demonstrate that, except for the effects of a few large earthquakes, most surface deformation is associated with interseismic strain accumulation, not coseismic strain release. If we assume that moment accumulation and release rates balance over long times, we can calculate the relative magnitudes of coseismic strain release (due to small earthquakes) and interseismic strain accumulation.

[11] The Gutenberg-Richter magnitude-frequency distribution is given by $\log_{10} N = a - bM_W$, where N is the cumulative number of earthquakes per year with magnitude greater than moment magnitude, M_W, and both a and b are constants. The scalar moment release from each earthquake is given by

$$M_0 = 10^{\alpha(M_W+\beta)}, \tag{1}$$

where $\alpha = 0.67$ and $\beta = 10.7$ (cgs units) [*Hanks and Kanamori*, 1979]. The total yearly moment release, Δ, due to all earthquakes up to magnitude M_W is given by the summation over all magnitudes multiplied by the magnitude frequency

$$\Delta(M_W) = \int_{-\infty}^{M_W} M_0(M'_W) N(M'_W) dM'_W. \tag{2}$$

We can compare the moment release due to small events (present in the geodetically observed velocity field) with the moment accumulation expected for larger events. All of the earthquakes less than or equal to M_W account for the fraction of total moment release given by

$$\lambda(M_W, M_W^{max}) = \frac{\Delta(M_W)}{\Delta(M_W^{max}) - \Delta(M_W)}, \tag{3}$$

Where M_W^{max} is the moment magnitude of the largest event. For southern California, we take the maximum size of an earthquake to be approximately the same size as the 1857 Ft. Tejon event ($M_W^{max} = 8.0$) [*Sieh*, 1978]. Thus all of the earthquakes up to $M_W = 5.0$, account for 3% (λ (5.0, 8.0) = 0.03) of the total moment release and the displacements due to small earthquakes ($M_W \leq 5.0$) are significantly smaller than the displacements associated with interseismic strain accumulation. *Ward* [1998] reached a similar conclusion.

3. Simple Models of the Earthquake Cycle

[12] A classic model for the upper crust and lower crust/upper mantle which captures the most fundamental rheological variations consists of two layers: a seismogenic elastic layer underlain by a Maxwell viscoelastic layer. This model has been used to study the time-dependent behavior of interseismic deformation. *Nur and Mavko* [1974] developed an approximate analytic solution for a dip-slip fault in order to model postseismic relaxation in Japan. *Savage and Prescott* [1978] developed an analytic model for periodic earthquakes on an infinitely long, vertical, strike-slip fault and *Savage* [2000] restated the solution in a more concise form. Recently, *Savage and Lisowski* [1998], *Segall* [2002], and *Dixon et al.* [2003] applied this model to interpret measurements of interseismic deformation in southern California.

[13] In a layered viscoelastic model, interseismic velocities depend on the material properties and the time elapsed since the last earthquake. The parameter that governs the time evolution is $\tau_0 = \mu T/2\eta = T/2\tau_M$, where μ is the shear modulus, T is the length of the earthquake cycle (recurrence interval), η is the dynamic viscosity of the viscoelastic layer, and τ_M is the Maxwell time. Although the explicit description of the time dependence is rather complicated [e.g., *Savage*, 2000], it is straightforward to characterize the variability of surface velocities on the basis of the parameter τ_0. For $\tau_0 > 1$, there are significant variations in the fault-parallel velocity profile through the seismic cycle (Figure 2). Velocities immediately following an earthquake are relatively fast and velocities late in the earthquake cycle are slow compared with the average velocity. The time dependent profiles nearly collapse onto the average profiles approximately 40% of the way through an earthquake cycle for values of τ_0 between 1 and 20.

[14] Large values of τ_0 may be due to either long repeat times or low viscosities. Conversely, for short repeat times ($T < 300$ years) and large viscosities ($\eta > 3 \times 10^{20}$) τ_0 is small ($\tau_0 < 0.5$). In this case there are negligible variations through the seismic cycle. The high viscosity limit is identical to the steady state expectation from a purely elastic model. *Savage and Burford* [1973] proposed a steady state interseismic deformation model for an infinitely long vertical strike-slip fault in a homogeneous elastic half-space. In

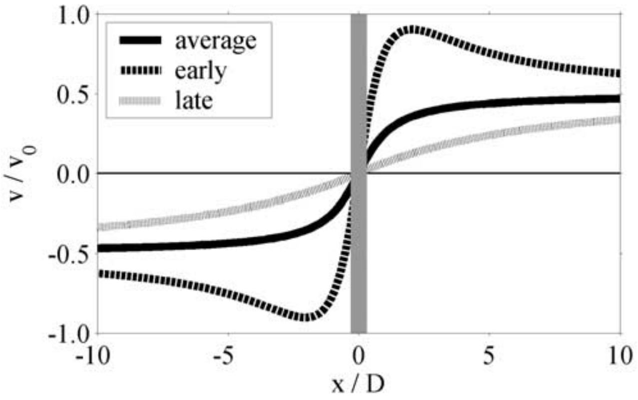

Figure 2. Fault-parallel velocities at different times in the seismic cycle following *Savage and Prescott* [1978]. The solid, dashed, and gray curves are the average, early, and late earthquake cycle velocity profiles. The time variation of these curves depends on the parameter $\tau_0 \approx 5$.

their model, the upper seismogenic layer is locked and a downdip extension of the fault zone creeps at a steady slip rate equal to the long-term geologic rate. In this model, the fault-parallel velocity profile is given by $v = v_0\pi^{-1} \tan^{-1} (x/D)$, where v_0 is the long-term slip rate, x is the distance from the fault trace, and D is the locking depth. The interseismic velocity profile is characterized by a smooth transition across the fault, in contrast to the coseismic and long-term geologic profiles, both of which are discontinuous across the fault (Figure 3). This model has been the basis for many interpretations of geodetically determined velocities and strain rates [e.g., *Savage and Burford*, 1973; *Bennett et al.*, 1997].

[15] If viscoelastic effects do contribute to interseismic velocity deformation, they may be mapped into a purely elastic model as variations in slip rate and locking depth [e.g., *Savage*, 1990; *Meade and Hager*, 2004]. Immediately after an earthquake, near-fault velocities are relatively high, and map into an elastic model as fast slip rates and shallow locking depths. Conversely, late in the earthquake cycle, relatively slow slip rates and deep locking depths would be inferred from an elastic model. If far-field velocities were available early in the earthquake cycle, and $\tau_0 > 1$, then the viscoelastic effect would be quite evident, as the velocity gradient would reverse approximately two locking depths away from the fault zone.

[16] We invoke the high viscosity (low τ_0) limit implicitly, which is equivalent to assuming that an elastic half-space model can adequately approximate the deformation of the viscoelastic Earth. An alternative assumption, with similar implications, is that the faults in southern California are, on average, approximately 40% of the way though their seismic cycles. We evaluate the validity of these assumptions later in this paper.

4. Block Modeling

[17] We divide southern California into blocks bounded by faults. To relate block motions and fault slip rates to geodetic observations of interseismic deformation, we start with the approach described by *Savage and Burford* [1973]. We extend and generalize this formulation to allow for the effects of block rotation on a sphere, dipping faults, finite length faults, and multiple blocks. For the two-dimensional case, the total block displacement over an earthquake cycle of length T is defined as the sum of the time-integrated interseismic velocity, $T\vec{v}_I$, and coseismic deformation contributions (Figure 3),

$$T\vec{v}_B = T\vec{v}_I(\vec{x}_S) + \vec{f}\left(\vec{d},\vec{x}_S,\vec{x}_F\right), \tag{4}$$

where $\vec{d}$ is the coseismic slip vector, $\vec{x}_S$ specifies geodetic station coordinates, and $\vec{x}_F$ represents the fault geometry. For an infinitely long strike-slip fault, the coseismic term is given by an arctangent function that depends on the distance from the fault and the elastic locking depth (Figure 3). If we divide equation (4) by T and assume that $\vec{f}$ is linear in $\vec{d}$ (i.e., linear elasticity), then we can pull the earthquake displacement out of the function $\vec{f}$. We can then write interseismic velocity as the difference between the block velocity and the yearly coseismic slip deficit (CSD) velocity,

$$\vec{v}_I = \vec{v}_B(\vec{x}_S) - \vec{v}_{\mathrm{CSD}}(\vec{x}_S,\vec{x}_F). \tag{5}$$

[18] Several studies have extended this argument from a single infinitely long fault to multiple finite faults in a planar formulation [e.g., *Matsu'ura and Jackson*, 1986; *McCaffrey*, 1996; *Souter*, 1998]. We move to a spherical framework, where we can directly estimate rotation vectors $\vec{\Omega} = (\Omega_x, \Omega_y, \Omega_z)$ for each block. *Murray and Segall* [2001] used a similar approach, ignoring fault-normal motion, for northern California and the Basin and Range province.

[19] We can write both $\vec{v}_B$ and $\vec{v}_{CSD}$ in terms of rotation vectors $\vec{\Omega}$. The block motion contribution to the interseismic velocity field is given by a rotation about an Euler pole

$$\vec{v}_B(\vec{x}_S) = \vec{\Omega} \times \vec{x}_S = \mathbf{R}_B(\vec{x}_S)\vec{\Omega}, \tag{6}$$

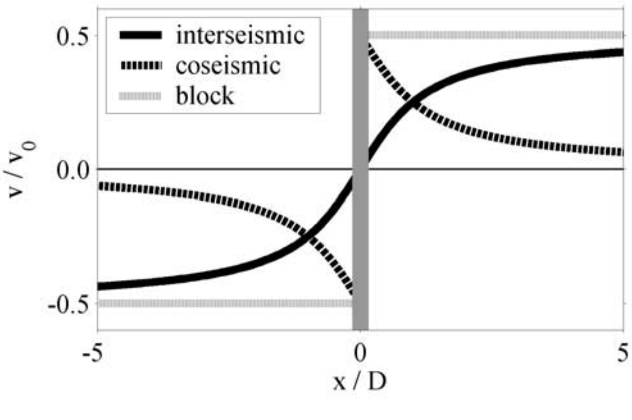

Figure 3. Fault-parallel velocity profiles across an infinitely long two-dimensional strike-slip fault, after *Savage and Burford* [1973]. The solid, dashed, and gray curves are the interseismic, coseismic, and interseismic velocity profiles. The vertical line is the fault trace. The block velocity is equal to the sum of the coseismic (slip deficit) and interseismic velocities. This is the simple case where the blocks on either side of the fault are translating past each other with only strike-slip motion on the fault.

where $\mathbf{R}_B(\vec{x}_S)$ is a linear cross product operator that is a function of station coordinates, $\vec{x}_S$, in Cartesian coordinates. One of the advantages of the block motion formulation over the traditional deep-slip model is that the effects of block rotations on the interseismic velocity field can be included (equations (5), (6)). This effect may significantly modify the classical arctangent profile such that the total far field velocity could be less than the fault slip rate [e.g., *Meade et al.*, 2002].

[20] To calculate the elastic (or coseismic slip deficit) contribution to the velocity field, we use *Okada*'s [1985] solutions for the surface deformation due to an arbitrarily inclined dislocation in a homogeneous elastic half-space. In order to use these formulas, we must project the fault geometry and station positions from spherical to planar geometry. While the spatial distortion due to a reasonable conformal projection over an area the size of southern California is <1%, the prospect of incorporating far-field velocities (e.g., plate interiors) motivated us to take a different approach to the "flattening" problem. It is important to model the elastic deformation accurately in the immediate vicinity of each fault, where the velocity gradients due to interseismic strain accumulation are largest. To accomplish this, we use a local projection for each fault segment, compute the elastic deformation rate, and rotate the velocities back into an east, north, up coordinate system. A locally tangent oblique Mercator projection allows us to flatten the spherical geometry in such a way that the trace of a fault segment is approximated as a great circle path between its two endpoints. Combining these transformations, we can write the slip deficit velocity as

$$\vec{v}_{\mathrm{CSD}} = \mathbf{R}_{X\rightarrow E}(\vec{x}_S)\mathbf{R}_P(\vec{x}_S, \vec{x}_F)\mathbf{R}_O(\vec{x}_S, \vec{x}_F)\vec{s}, \tag{7}$$

where $\mathbf{R}_{X\rightarrow E}$ transforms XYZ velocities to an ENU (east, north, up) coordinate system, $\mathbf{R}_P$ projects the station and fault positions into planar space from their spherical coordinates, and $\mathbf{R}_O$ contains the partial derivatives of *Okada*'s [1985] elastic Green's functions with respect to slip rate. The fault slip rates are linearly related to the rotation vectors by,

$$\vec{s} = \mathbf{R}_F(\vec{x}_F)\mathbf{R}_{\Delta v}(\vec{x}_F)\vec{\Omega}, \tag{8}$$

where $\mathbf{R}_{\Delta v}$ projects the rotation vectors into a relative velocity at the fault midpoint. Thus, for a given set of rotation vectors, $\mathbf{R}_{\Delta v}\vec{\Omega}$ gives the two components of the relative velocity vector $\Delta\vec{v} = (\Delta v_{\|}, \Delta v_{\perp})$. $\mathbf{R}_F$ is a linear operator that projects the relative velocity onto the fault plane. By substituting equation (8) into equation (7), fault slip rates can be written as a function of a set of rotation vectors. Because the fault slip rates are functions of the rotation vectors, they are not free to vary independently, and the block geometry provides kinematic constraints on how slip rates covary. Thus, relative to a method where the slip rates are independent of each other [e.g., *Hubert-Ferrari et al.*, 2000], the block model approach reduces the covariance between locking depth and slip rate by reducing the number of correlated model parameters, as there are far fewer blocks than fault segments.

[21] While a dislocation can have three components of slip (strike, dip, and tensile, alternatively $s_{\|}$, s_δ and $s_\perp$), we only allow two components of slip for each fault. The strike-slip component is equal to the projection of the relative velocity vector along the fault azimuth. Vertical faults have a tensile-slip component equal to the convergence rate. The horizontal displacement field generated by a vertical tensile dislocation is similar to the horizontal displacement field generated by a pair of conjugate thrust faults [*Souter*, 1998]. In our model, the tensile component of deformation is a coarse parameterization of compression and extensional structures adjacent to predominantly strike-slip boundaries. Faults with dips other than 90° have no tensile-slip but, instead, have a dip-slip component. For a given convergence rate, the dip-slip rate on a nonvertical fault increases with dip. The relationship between the fault-normal components of the relative block velocity vector to the nonstrike-slip rates is

$$\Delta v_\perp = \begin{cases} s_\perp & \text{if } \delta = 90^\circ \\ s_\delta \cos\delta & \text{if } \delta \neq 90^\circ \end{cases}. \tag{9}$$

As the fault slip rates are projections of relative block motion vectors, the fault slip rates are internally consistent, and the surface velocity field implicitly satisfies a velocity path integral constraint on both geodetic and geologic timescales. That is, the relative motion between any two points does not depend on the path between them. This constraint is an implicit feature of the block model and ensures that we generate internally consistent slip rate estimates.

[22] We substitute equations (6), (7), and (8) into (5) to write the interseismic velocities in terms of a single multiplication, $\vec{v}_I = (\mathbf{R}_B - \mathbf{R}_C)\vec{\Omega}$, where $\mathbf{R}_C$ is a combination of the matrices in equations (7) and (8). While our study is primarily concerned with inverting geodetic data for block motions, the method presented above also affords the possibility to include both a priori slip rate and plate motion estimates into the same inversion. The system of equations defining the forward problem can be written as:

$$\begin{pmatrix} \vec{v}_I \\ \vec{s} \\ \vec{\Omega} \end{pmatrix} = \begin{pmatrix} \mathbf{R}_B - \mathbf{R}_C \\ \mathbf{R}_F\mathbf{R}_{\Delta v} \\ \mathbf{I} \end{pmatrix} \vec{\Omega}, \tag{10}$$

where $\mathbf{I}$ is the identity matrix. In general, we are interested in the inverse problem where we have to estimate $\vec{\Omega}_{\mathrm{est}}$ from observations. If we write equation (10) as $\vec{d} = \mathbf{R}\vec{\Omega}$ (where $\vec{d}$ represents the data and $\mathbf{R}$ the Jacobians) then we can estimate a set of rotation vectors by minimization of the sum of weighted least squares

$$\vec{\Omega}_{\mathrm{est}} = \left(\mathbf{R}^{\mathbf{T}}\mathbf{W}\mathbf{R}\right)^{-1}\mathbf{R}^{\mathbf{T}}\mathbf{W}\vec{d}, \tag{11}$$

where $\mathbf{W}$ is the combined weighting matrix. This matrix contains the weights for each of the data sets (observed velocities, slip rates, a priori block motions),

$$\mathbf{W} = \begin{pmatrix} \beta_G\mathbf{W}_G & 0 & 0 \\ 0 & \beta_s\mathbf{W}_s & 0 \\ 0 & 0 & \beta_\Omega\mathbf{W}_\Omega \end{pmatrix}, \tag{12}$$

where each of the $\mathbf{W}$'s on the right hand side of equation (12) is the inverse of the covariance matrix associated with each data set. We treat covariance matrices as diagonal. Each of the β's in equation (12) is a coefficient that sets the relative weights for each data set. These parameters are useful when there is an imbalance between the number of equations representing geodetic data and the number of a priori slip rate estimates. We estimate the slip rates, $\vec{s}_{\mathrm{est}}$, by substituting $\vec{\Omega}_{\mathrm{est}}$ into equation (8). Formal slip rate uncertainties are calculated by propagating the estimated rotation vector uncertainties through equation (8). The Euler pole location and rotation rate uncertainties are calculated by Monte Carlo propagation so that we do not have to linearize the conversion from rotation vector to Euler pole space.

[23] We can also include a priori plate motion or slip rate estimates in the inversion. This provides us with a consistent framework for performing joint inversions of geologic and geodetic data. While we focus on the geodetic data in this paper, we have used some constraints to eliminate "checkerboard" deformation. This behavior consists of an alternating pattern of large amounts of convergence and divergence along what are thought to be predominantly strike-slip faults. While the magnitude of normal motion may be large on any one of these faults, the sum across the fault system is small. We find that "checkerboarding" occurs along the faults bounding a series of long, thin blocks, such as those south of Los Angeles and in the Eastern California Shear Zone. To minimize this artifact of the inversion, we have added several constraints that limit the normal motion on faults that otherwise show "checkerboard" behavior.

5. Geodetic Data

[24] The southern California Earthquake Center Crustal Motion Map 3.0 (SCEC CMM 3.0; Shen et al., crustal motion map, 2003) provides the current consensus estimate of horizontal interseismic velocities at the regional scale in southern California. Most of the data are survey-mode GPS, with some of the older stations having time series that span nearly ten years. During the period of GPS observations, there have been three large earthquakes in southern California: the $M_W = 7.3$ Landers earthquake (1992) in the southern Mojave Desert; the $M_W = 6.7$ Northridge (1994) event on the southern edge of the Ventura Basin; and the $M_W = 7.1$ Hector Mine (1999) earthquake, which ruptured about 40 km to the east-northeast of the Landers epicenter. Coseismic and postseismic deformation from these earthquakes has made it difficult to evaluate some of the longer time series for interseismic deformation. The SCEC CMM 3.0 includes coseismic displacement models to correct time series for earthquake deformation. It also attempts to remove postseismic deformation by eliminating 1.5 years of data following Landers and Hector Mine events, although additional long-term relaxation effects may still be present in the geodetic data. We discuss this possibility later in the context of the block model results.

[25] The SCEC CMM 3.0 contains estimated velocities for 840 stations with observations through 2001. We combined this data set with three others by solving for the set of rotation vectors that would best align the velocities at common stations independent of the block model. To ensure that we model the Pacific plate motion adequately, we combined the SCEC velocities with the far-field velocities reported by *Steblov et al.* [2003]. We added four stations from the BARD network that lie on the northern extension of the Sierra Block (UCD1, SUTB, QUIN, and ORVB [*Murray and Segall*, 2001]). These sites were required to produce a robust estimate of the Sierra Block motion, and, thus, the central San Andreas fault slip rate. To increase data coverage in the ECSZ, we used an update of the station velocities reported by *McClusky et al.* [2001] (S. McClusky, personal communication, 2004). *McClusky et al.*'s [2001] analysis (including longer time series) yields smaller uncertainties than most of the campaign-mode data in the SCEC CMM 3.0 velocity field. To minimize potential bias due to different weighting schemes in the data processing, we increased the *McClusky et al.* [2001] uncertainty estimates by ~0.4 mm/yr so that the median uncertainty was the same as that in the SCEC CMM 3.0. For the small number of far field stations (Pacific plate, northern California), we use the reported velocity uncertainty estimates.

[26] We reduced the number of stations used in the inversion based on different quality criteria. First, we eliminated all velocities with east or north velocity uncertainties larger than 1.5 mm/yr. These stations tend to clutter the residual velocity field yet contribute minimally to constraining block motions due to large uncertainties. For some stations near the 1992 Landers and 1999 Hector Mine rupture zones, postseismic deformation is evident for at least two years after these events [*Pollitz et al.*, 2000]; such sites were eliminated. We chose not to use the EDM velocities in the SCEC CMM 3.0 field because the network tie relationships were not clear. Preliminary models showed residual velocities at EDM stations with coherent patterns relative to nearby GPS sites. These may be related to network tie problems (not accounted for by our assumed diagonal covariance matrix) that are easy to confuse with block motions. VLBI sites tend to have small formal uncertainties, but their velocities often depart significantly from collocated GPS stations. Because this systematic difference is not understood we chose to eliminate all VLBI sites in favor of a uniform GPS data set. Some velocity estimates are also affected by nontectonic signals, such as subsidence related to anthropogenic activity [e.g., *Bawden et al.*, 2001]. Stations in the immediate vicinity of Parkfield were eliminated as the fault at the junction of the locked and creeping sections of the SAF is partially creeping [e.g., *Murray et al.*, 2001], whereas we assume that a fault is either fully locked or creeping. We also eliminated stations in regions that were outside of our study area, such as those in the San Francisco area and the Basin and Range province. In the ECSZ, we eliminated stations near the COSO geothermal field near the Airport Lake fault because of substantial motions associated with production. We also eliminated stations that are thought to have local site effects (AGUE, 0501). The last step in reducing the velocity field was an iterative elimination of outliers with residual velocities that tended to dominate the minimization criteria (i.e., contribute more than 5%). This involved examining the residual velocities from the block model and identifying stations that were anomalous compared to their neighbors. Most of these stations are along the southern SAF between the Salton Sea and the Cerro Prieto fault. After this procedure, our combined velocity field has 439 stations with a mean uncertainty magnitude of 1.45 mm/yr.

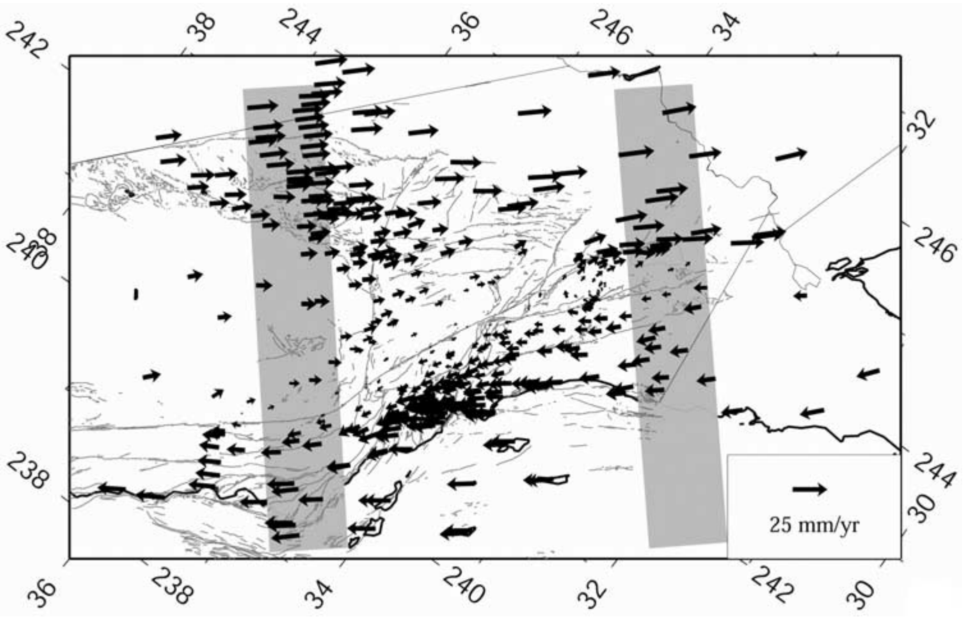

Figure 4. Observed interseismic velocities in southern California from GPS measurements. No confidence ellipses are shown in order to reduce clutter. The map projection is a locally tangent oblique Mercator with the azimuth oriented approximately parallel to the SAF. The velocities are in a mean southern California reference frame. The shaded swaths are the regions in which the fault parallel velocities are drawn (Figure 5). The light gray lines are fault traces from *Jennings* [1994].

[27] Figure 4 shows our combined interseismic velocity field in a southern California reference frame defined to have an average velocity of zero. Stations on the North American plate move toward the southeast, while those on the Pacific plate move toward the northwest at about half of the relative plate velocity. The observed velocities do not jump abruptly across the SAF, but instead vary smoothly (Figures 4 and 5). The gradual transitions across the fault zones are similar to the simple interseismic velocity model shown in Figure 3. Note that while each of the profiles shows approximately the same total velocity change (~42 mm/yr) from the Pacific to the North American plates, the gradients are quite different. In the northern profile, the fault-parallel velocity drops by about ~30 mm/yr across the SAF. Through the San Joaquin Valley, the velocity gradient flattens out before distributing ~12 mm/yr across the ECSZ. In contrast, the southern profile shows no intermediate flattening and the total velocity drop occurs across a distance that is about 50% that in the northern profile. This reflects the difference in the fault system geometry from north to south. The flat portion of the northern profile reflects the relative stability of the ~200 km wide Sierra Block, with the actively deforming central SAF to the west and ECSZ to the east. In contrast, the southern profile shows that approximately 80% of the relative plate motion is accommodated across the SAF and SJF, separated by only ~40 km.

6. Southern California Block Geometry

[28] The large number of active faults in southern California led us to develop a relatively complex block model compared to the other regions that we have studied, the Tien Shan in Central Asia [*Meade and Hager*, 2001] and

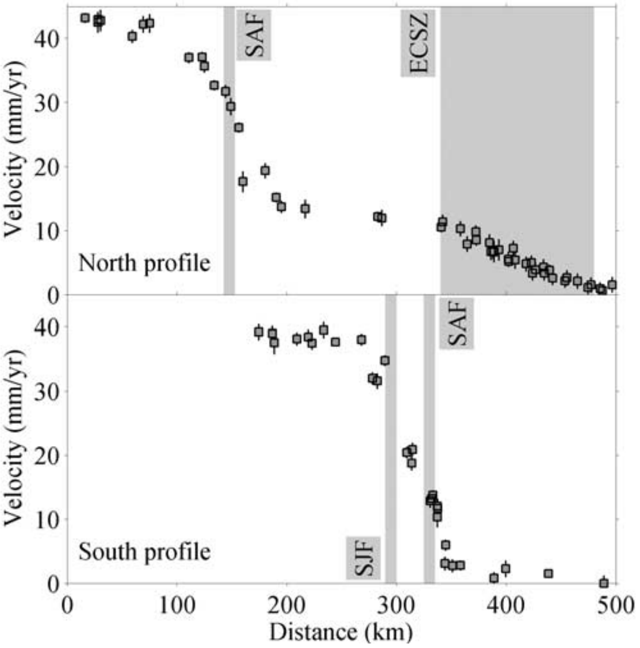

Figure 5. Fault-parallel velocities from the northern and southern swaths, respectively shown in Figure 4. The vertical lines give the 1σ fault-parallel velocity uncertainty estimates. The gray shaded areas show the locations of the SAF: San Andreas fault (SAF), San Jacinto fault (SJF), and Eastern California Shear Zone (ECSZ). The total change in velocity across both profiles is approximately 42 mm/yr, but the transition occurs over a shorter distance in the southern profile because of the close spacing of the SJF and SAF.

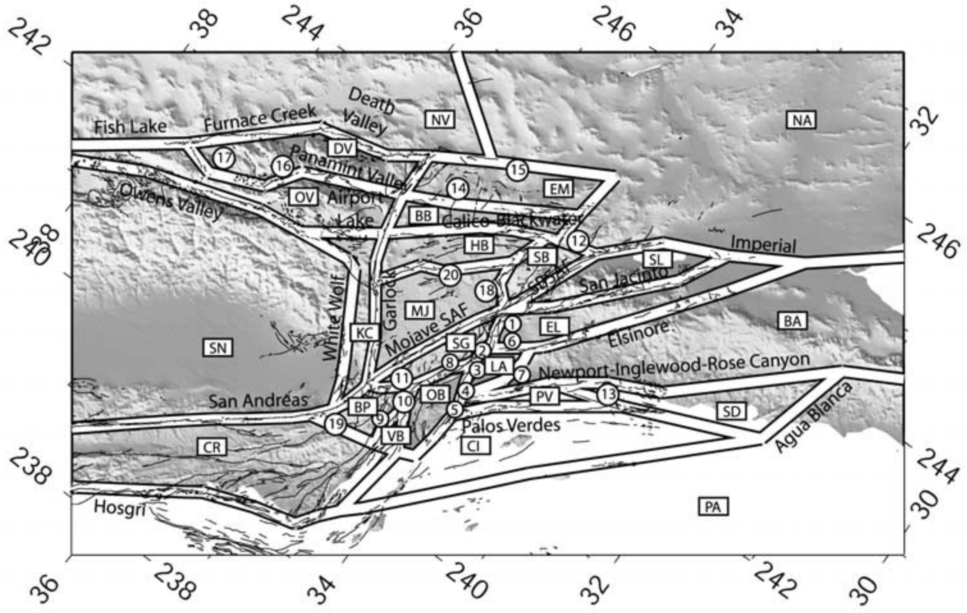

Figure 6. Topography (GTOPO30), fault traces (thin black lines [*Jennings*, 1994]) and model block boundaries (thick lines) in and around southern California. The map projection allows the San Andreas fault to be horizontal outside of the Big Bend. North is toward the top left corner. The 24 blocks in our preferred model are labeled (rectangles): Baja (BA), Blackwater (BB), Big Pine (BP), Coast Islands (CI), Coastal Ranges (CR), Death Valley (DV), Elsinore (EL), Eastern Mojave (EM), Helendale (HB), Kern County (KC), Los Angeles (LA), Mojave (MJ), North America (NA), Oakridge (OB), Owens Valley (OV), Nevada (NV), Pacific (PA), Palos Verdes (PV), San Bernadino (SB), San Diego (SD), San Gabriel (SG), Salton (SL), Sierra Nevada (SN), Ventura Basin (VB). Selected fault names are labeled directly on the fault. Circled numbers refer to the following faults: Cucamonga (1), Sierra Madre (2), Raymond Hill (3), Hollywood Hills (4), Santa Monica Mountains (5), Chino (6), Puente Hills (7), Santa Susana (8), San Cayetano (9), Oakridge (10), San Gabriel (11), Eureka Peak (12), Oceanside (13), Goldstone (14), Mojave East (15), Hunter Mountain (16), Saline Valley (17), North Frontal (18), Coastal Ranges Split (19), Helendale (20).

the North Anatolian fault zone [*Meade et al.*, 2002]. We adopt a model with 24 blocks (Figure 6). These blocks range in size from plate scale (e.g., Pacific and North American blocks) to structure scale (Ventura Basin block, Figure 7). The block boundaries coarsely represent structures that are more complicated in the real world. These idealizations are most evident in the Los Angeles and Ventura basins, where we have simplified the complex system of dipping faults to create simply connected block boundaries (Figure 7). We are unable to separate the compound effects of faults that are very close to each other (e.g., San Jose and Sierra Madre fault zones near the San Gabriel range front). However, St. Venant's principle [e.g., *Malvern*, 1969] assures that the elastic effects away from the fault zone are not sensitive to the details of the locked geometry. For this reason, the block boundaries used here are smoother than the corresponding faults on the *Jennings* [1994] map.

[29] We arrived at this preferred model by an iterative procedure, starting with the *Jennings* [1994] fault map and the work of previous authors [*Bird and Rosenstock*, 1984; *Bird and Kong*, 1994; *Bennett et al.*, 1996; *Souter*, 1998]. We modified the block model boundaries to minimize the residual velocities and conform to some of our geologic/tectonic prejudices. This allowed us to develop a model that is compatible with much of the mapped SCFS geometry and

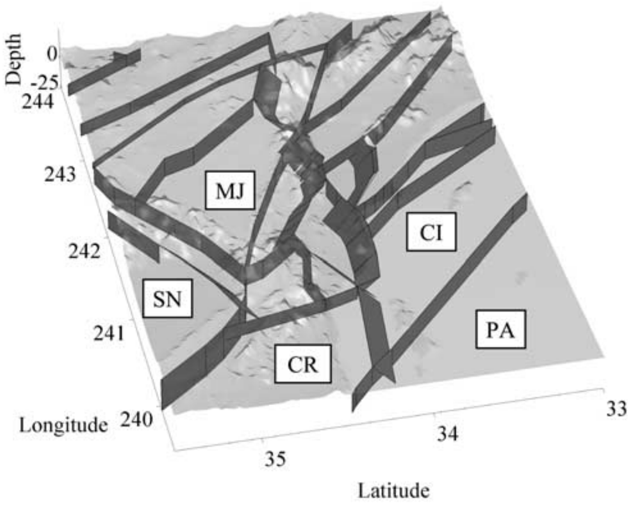

Figure 7. Topography and block model geometry of our preferred model focused on the Los Angeles region. The view is from the west-northwest. All nonvertical faults dip at 45°. The Coast Islands (CI), Coastal Range (CR), Mojave (MJ), Pacific (PA), and Sierra Nevada (SN) blocks are labeled for reference.

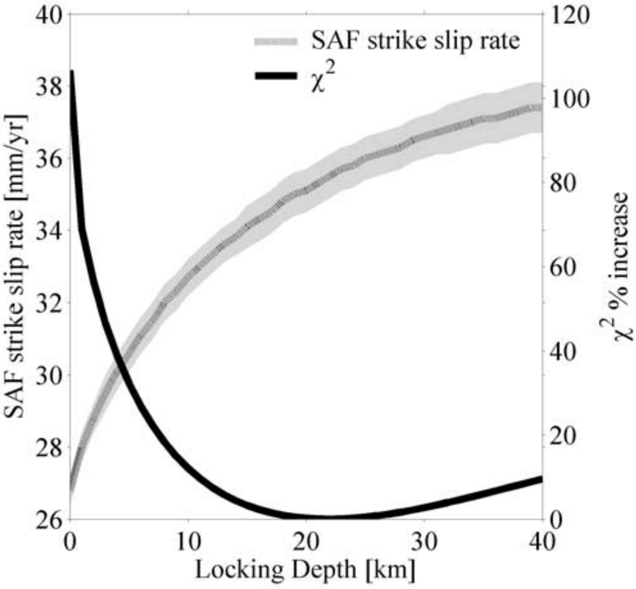

Figure 8. Fit to data (right axis) and slip rate (left axis) on the Carrizo segment of the San Andreas Fault (CSAF) as a function of the CSAF locking depth. The solid black line shows the fit (χ^2) as a function of CSAF locking depth, with a minimum at 25 km. The monotonically increasing dashed curve shows the CSAF strike-slip rate as a function of CSAF locking depth and gray shaded region indicates the slip rate uncertainty at each locking depth. The uncertainties become larger with increasing locking depth because the elastic deformation zone broadens around the fault and the correlation between the estimated model parameters (rotation vectors) increases. Our preferred slip rate for the Carrizo segment of the SAF is the slip rate at the locking depth that minimizes the χ^2_ν. This corresponds to 35.9 ± 0.7 mm/yr at a CSAF locking depth of 25 km.

geodetic observations of interseismic deformation. However, we did introduce at least one feature that has no commonly recognized geologic analog: the Coastal Ranges split. Without the division between the Coastal Ranges and Big Pine block (Figure 6, structure 19), the residual velocity field north of the Ventura Basin and west of the central San Andreas fault has coherent southerly and northerly velocities respectively. With the structure that separates the Coastal Ranges and Big Pine blocks included, the residuals are significantly reduced, and we recover both substantial shortening along the northern edge of the Ventura Basin and a right-lateral strike-slip rate greater than 30 mm/yr on the central San Andreas fault. We chose the number of blocks in our preferred model by modifying the geometry to minimize coherent residual velocities, while maintaining reasonable goodness of fit statistics. With very small blocks (<1000 km^2), the correlations between model parameters increase as the effects of elastic strain accumulation dominate the block motion contribution to the velocity field. Our preferred model includes the following 24 blocks: Baja (BA), Blackwater (BB), Big Pine (BP), Coast Islands (CI), Coastal Ranges (CR), Death Valley (DV), Elsinore (EL), Eastern Mojave (EM), Helendale (HB), Kern County (KC), Los Angeles (LA), Mojave (MJ), North America (NA), Oakridge (OB), Owens Valley (OV), Nevada (NV), Pacific (PA), Palos Verdes (PV), San Bernadino (SB), San Diego (SD), San Gabriel (SG), Salton (SL), Sierra Nevada (SN), and Ventura Basin (VB).

7. Results and Interpretation

7.1. Locking Depth Variations

[30] The choice of locking depth determines the third dimension of the fault system geometry. With elastic dislocation models, deeper locking depths lead to strain distributed over wider zones. Given that we do not know the locking depths a priori, and that our homogeneous elastic model may misrepresent locking depth in the presence of variable elastic structure [e.g., *Rybicki*, 1971; *Hager et al.*, 1999], we decided to estimate the effective locking depths of critical fault segments. This also allows us to interpret locking depths in terms of a viscoelastic earthquake cycle [e.g., *Savage*, 1990; *Savage and Lisowski*, 1998; *Meade and Hager*, 2004].

[31] Our preferred model has locking depth variations from 0–25 km. The SAF and SJF have rapid enough slip rates and dense enough station coverage that we can estimate locking depths by direct forward modeling. For the remaining faults, we used the results of previous studies, where available, or a default value of 15 km. *Peltzer et al.* [2001] estimated a very shallow locking depth (~5 km) for the Blackwater fault, and we use the same value for consistency. For all other faults in the ECSZ, we used a 10 km locking depth, as suggested by *McClusky et al.* [2001]. The Northridge earthquake in the Ventura Basin ruptured to a depth of 18 km, providing an objective estimate for the local locking depth near the Oakridge fault. However, *Donnellan et al.* [1993a, 1993b] found that a 5 km locking depth in an elastic half-space model could best fit two-dimensional profiles of fault normal velocities in this same region. *Hager et al.* [1999] demonstrated that this shallow locking depth mimics the effects of the lateral shear modulus variations in the Ventura Basin region. We use a 5 km locking depth in our model, but interpret it as a proxy for a deeper locking depth in the earth. Experiments with a range of locking depths have shown that the residual velocities along the southern SCFS are best fit by a creeping Imperial fault, and relatively shallow SJF and southern SAF locking depths (10 and 15 km respectively).

[32] The fault locking depth that most directly affects both the fit to the data and the estimated fault slip rates is that of the Carrizo SAF (CSAF), from Parkfield to its intersection with the Garlock fault. This is the northern half of the 1857 Ft. Tejon earthquake rupture zone [e.g., *Sieh*, 1978]. Figure 8 shows how the geodetic data fit the model for a range of CSAF locking depths from 0 to 40 km. These statistics were calculated by doing separate inversions for each locking depth. The fit is best at approximately 25 km depth, with very shallow locking depths fitting the data very poorly ($\chi^2|_{D=0}/\chi^2|_{D=25} = 2.1$). The gray curve in Figure 8 shows how the strike-slip rate along the CSAF varies with locking depth. For the best fitting locking depth, the CSAF slips at 35.9 ± 0.9 mm/yr. Shallower locking depths may underestimate the fault slip rate by as much as 10 mm/yr. Formal slip rate uncertainties grow as a function of locking depth as the block motions become more coupled due to

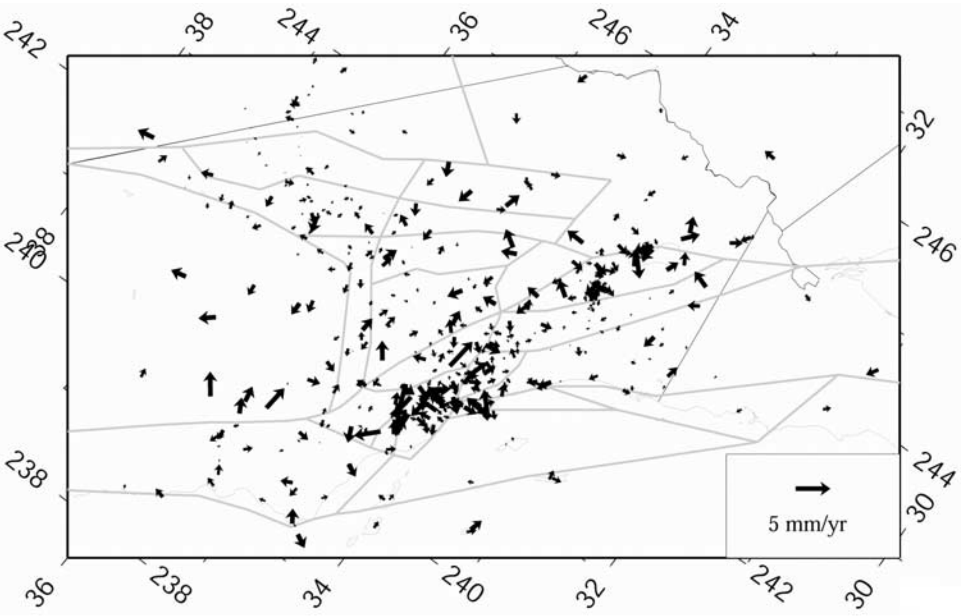

Figure 9. Residual (observed-model) velocities. The gray lines show the block model fault traces. Note that the velocity vectors on this figure are drawn at a scale that is five times larger than the observed velocity vectors shown in Figure 4. This uncertainty is just smaller than the mean of the combined observations. Seventy-two percent of the residual velocities are smaller than their 1-σ uncertainty estimates.

the broadening of the strain accumulation zone. In the end-member case, where all the faults have zero locking depth, there is no coupling between the blocks, and the only contribution to the slip rate uncertainties is from the data uncertainties. Experiments with synthetic data and two-dimensional models show that the asymmetry about the minimum in the $\chi^2(D)$ curve is due to the decrease in the sensitivity with increasing locking depth ($\partial v/\partial D < 0$). Thus, our CSAF locking depth estimate is consistent with what we would expect from an optimal estimate. In contrast, a deep locking depth for the Mojave SAF does not significantly change the fit to the data, though there is a strong covariance between slip rate and locking depth (i.e., slip rate increases with locking depth).

[33] We find that the SAF just to the east of the Salton Sea is fit best by a 15 km locking depth. In contrast, *Lyons and Sandwell* [2003] found that only the portion of the fault from 3 to 8 km appeared locked. This may reflect a bias in one of the data sets, for example, the inclusion of GPS velocities affected by transient postseismic deformation following the Landers and/or Hector Mine earthquakes. There may be less of a postseismic signature in the radar data used by *Lyons and Sandwell* [2003].

7.2. Fit to Data

[34] Our preferred model is able to account for most of the features in the observed velocity field, with a mean residual magnitude of 1.26 mm/yr (Figure 9). The velocity χ^2/DOF = 1.05, and 72% of the residual velocity components are smaller than their 1-σ uncertainty estimates. There is a weak correlation between the rate of elastic strain accumulation and the residual velocity magnitude (0.19 ± 0.04 at the 67% confidence level). The relationship between residual velocity magnitude and contribution to the minimization criteria (χ^2) is not linear (Figure 10). The scatter from the main diagonal band in Figure 10 highlights the fact that a station with a smaller residual velocity may contribute more to the overall minimization criteria than a station with a larger residual, due to the differences in the estimated uncertainties. For example, TAR0 has a residual velocity magnitude 0.3 mm/yr smaller than GOUD, but contributes 87% more to the minimization criterion due to smaller estimated velocity uncertainties. Both of these stations, and two of their neighbors (C616 and P807) east of the CSAF on the Sierra block, have eastward directed residuals, suggesting the need of for motion normal to the direction of relative plate motion on a structure east of the SAF.

[35] Coseismic or postseismic deformation may explain some coherent residuals. The SCEC CMM 3.0 uses coseismic deformation models to span across the Landers, Northridge, and Hector Mine earthquakes in order to recover longer time series. Given that coseismic displacement models are generally not accurate to the centimeter level within a few rupture depths of the epicenter, we have reason to suspect coherent residuals in the immediate vicinity of an earthquake with station time series that span the event. Some of the residual velocities near the Northridge epicenter share the same sense of motion as the coseismic displacements (Figures 9 and 11). Short-term postseismic deformation following large earthquakes may persist at the mm/yr level for more than two years after the coseismic rupture [e.g., *Pollitz et al.*, 2000]. The SCEC CMM 3.0 eliminates 1.5 years of data following the Landers earthquake at about 30 near-field stations (Shen et al., crustal motion map, 2003). There is no correction for longer-term postseismic deformation. Either of these explanations may

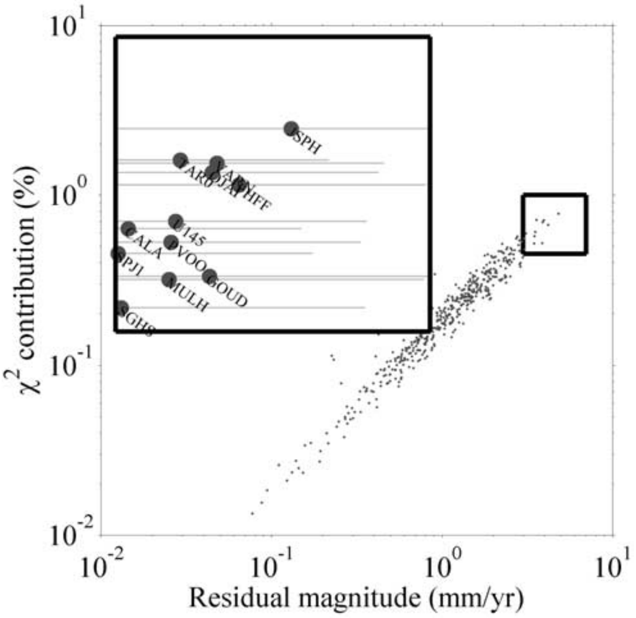

Figure 10. The relationship between the magnitude of the residual velocity vectors and their contribution to the minimization criteria. To calculate the contribution to the fit criteria we sum the weighted squared magnitude at each station and then normalize by the total number of stations. The thick dark lines indicate a zoomed in region where we highlight the names of the station that contribute most.

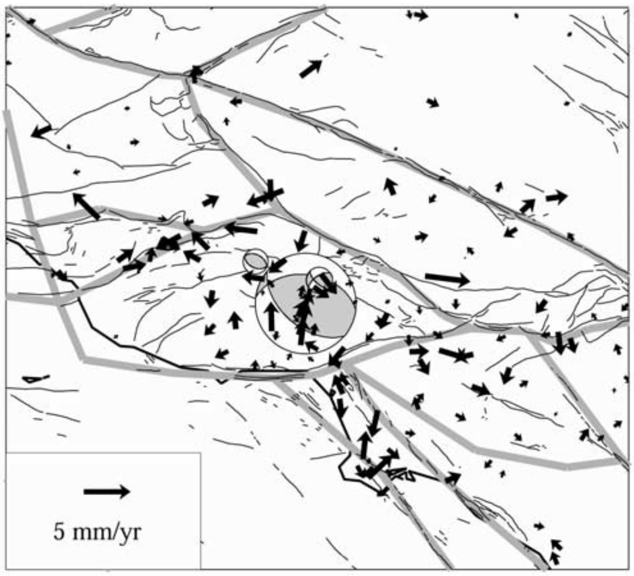

Figure 11. Residual velocities in the greater Los Angeles area with Harvard CMT focal mechanisms for the 1994 Northridge earthquake and large aftershocks.

account for systematic residuals near the Landers and Northridge earthquakes (Figures 9 and 11).

7.3. Pacific-North America Euler Pole

[36] The most basic measure of the integrated deformation between the Pacific and North American plates is their relative Euler pole (Table 1). Our Euler pole location is east of some recent estimates. This is likely due to our inclusion of more stations on the North American plate compared with previous studies [e.g., *Sella et al.*, 2002]. The difference in Euler Pole location and rotation rate can account for ~3 mm/yr of differential motion across the SCFS. We also estimated the PA-NA Euler pole using a traditional plate model with no elastic deformation and only those stations in the centers of the Pacific and North American plates. With no elastic deformation and fewer stations, the Euler pole longitude shifts 3° eastward; closer to previous estimates [e.g., *DeMets and Dixon*, 1999; *Argus and Gordon*, 2001; *Sella et al.*, 2002].

7.4. Estimated Slip Rates

[37] In our block model formulation, slip rates are linearly related to the rotation vectors (equation (8)). Figures 12 and 13 show the strike-slip and "fault-normal" slip rates. The "fault-normal" components are tensile if the fault is vertical and dip-slip otherwise. Reported slip rates have been calculated at the nearest segment midpoint. Formal uncertainties range from 0.5 to 3.2 mm/yr (Table 2). Faults bounded by large blocks tend to have smaller uncertainties (e.g., central SAF). Experience with a range of models has shown that the uncertainties due to variations in fault system geometry are larger than the formal slip rate uncertainties from a given inversion. In practice, the reported slip rate uncertainties should be scaled upward to reflect the uncertainty in fault system geometry. We suggest that ±3 mm/yr is an appropriate empirical uncertainty for most faults.

7.5. San Andreas Fault System

[38] The SAF is the fastest slipping fault in our model, with the northernmost (Parkfield) and southernmost (Cerro Prieto) sections moving at 36.0 ± 0.5 and 40.0 ± 1.5 mm/yr, respectively (Figure 12 and Table 2). As the Imperial fault merges with the SAF, it transfers 2.7 ± 0.6 mm/yr of strike-slip motion to the Elsinore fault and 11.9 ± 1.2 mm/yr to the San Jacinto fault at their intersection to the south of the Salton Sea. Farther north, the SAF slows further as it feeds 21.3 ± 1.6 mm/yr of strike-slip motion into the ECSZ through the Eureka Valley fault. This is largely facilitated

Table 1. A Compilation of Estimated Pacific–North America Euler Pole Locations and Rotation Rates, Including the Estimate From Our Block Model[a]

Source	Longitude	Latitude	Rotation Rate
NUVEL-1A	−78.2 ± 1.3	48.7 ± 1.2	0.750 ± 0.010
DeMets and Dixon [1999]	−73.7 ± 2.0	51.5 ± 1.0	0.765 ± 0.016
Argus and Gordon [2001]	−75.9 ± 0.8	50.1 ± 0.4	0.778 ± 0.014
Sella et al. [2002]	−72.1 ± 0.6	50.4 ± 0.4	0.755 ± 0.004
This paper (block model)	−78.9 ± 0.4	50.6 ± 0.3	0.782 ± 0.003
This paper (plate)	−76.9 ± 0.3	50.4 ± 0.2	0.785 ± 0.003

[a] Longitude and latitude are given in degrees, and rotation rate is given in degrees per million years. Our uncertainty estimates were calculated using a Monte Carlo method to convert from rotation vector covariance (directly estimated in the inversion) to a set of Euler Pole locations and rotation rates. The nonlinear approach tends to reduce the rotation rate uncertainty and increase the pole location uncertainties compared with the linear uncertainty propagation. The block model estimate includes many stations on the North American plate in southern California that are affected by the elastic strain accumulation model. In contrast, the plate motion estimate from this paper includes no elastic deformation and only those stations far from the boundaries of the Pacific and North American plates.

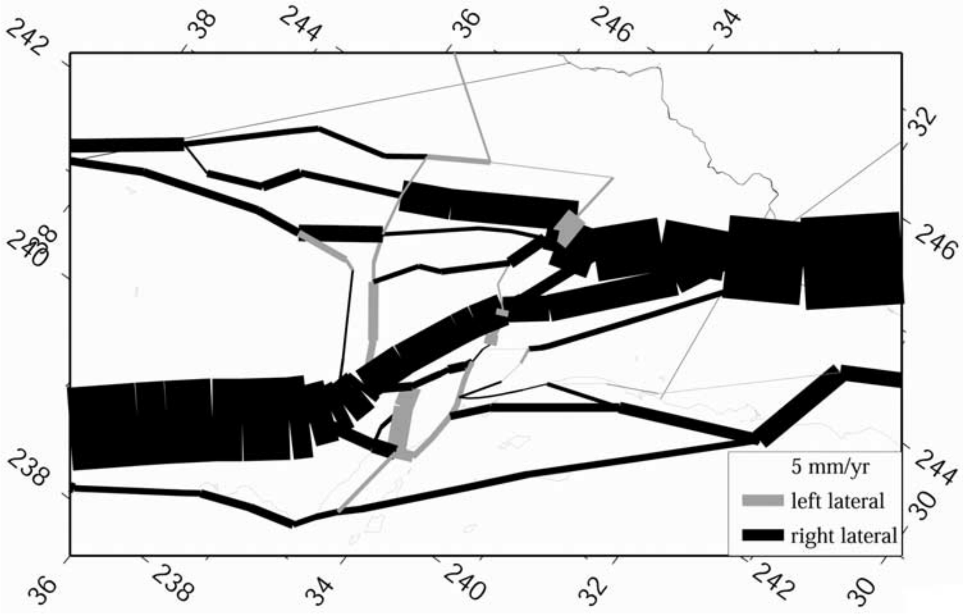

Figure 12. The estimated strike-slip rates from our preferred block model. Black and gray lines indicate right- and left-lateral motion, respectively. Wider lines indicate faster slip rates. The thickest lines represent the SAF and SJF where ~70% of the relative plate motion is accommodated.

by the counterclockwise rotation of the San Bernadino (SB) block. Without the SB block included, the Eureka Peak slip rate is 16.3 ± 0.4 mm/yr. This series of fault intersections along the southern SAF leaves only 5.1 ± 1.5 mm/yr of right-lateral motion on the San Bernadino segment near the San Gorgonio Pass. Shortening (1.0 ± 1.7 mm/yr) along the San Bernadino segment of the San Andreas fault is a consequence of the Salton block impinging upon the southern edge of the SB/MJ block. Along the Mojave segment, the SAF slips at 14.3 ± 1.2 mm/yr, due to rejoining with the SJF. The Mojave SAF slip rate covaries, and increases, with locking depth. As the SAF bends to the north and emerges out of the Big Bend, a 25 mm/yr right-lateral strike-slip rate is complemented by ~5 mm/yr of shortening. This is due to the Big Pine block impinging on the southern boundary of the Sierra Block. The White Wolf

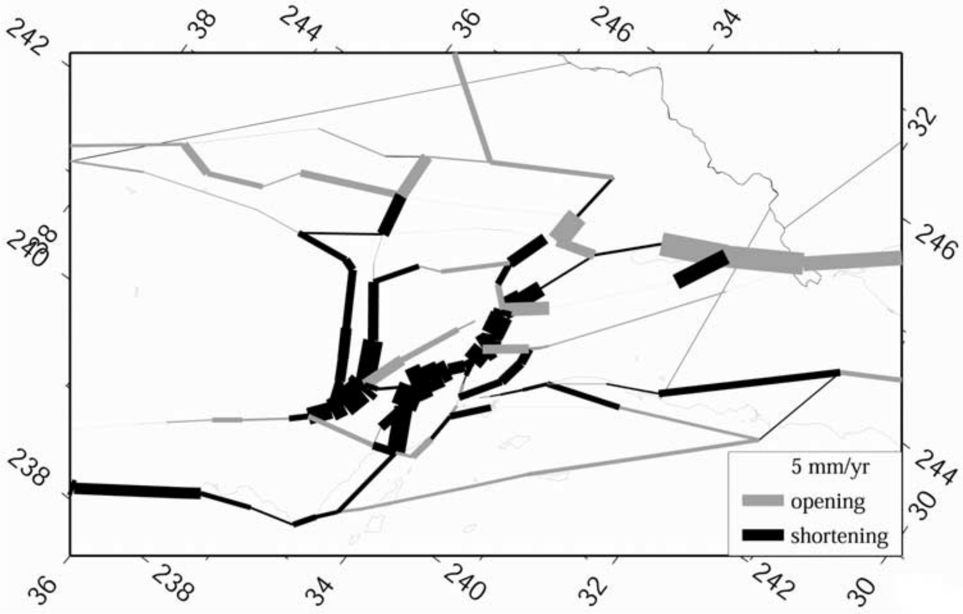

Figure 13. The estimated dip- and tensile-slip rates from our preferred block model. Black and gray lines indicate closing and opening, respectively. Wider lines indicate faster slip rates. Slip rates are tensile-slip for vertical faults and dip-slip otherwise. The only faults that dip are those around the Los Angeles area (see Figure 7 and Table 2).

Table 2. Selected Fault Slip Rates From Our Preferred Block Model[a]

Fault Name	Strike-Slip Rate	Dip-Slip Rate	Tensile-Slip Rate	Locking Depth
SAF (Parkfield)	36.0 ± 0.5	. . .	0.1 ± 0.4	1
SAF (Carrizo)	35.9 ± 0.7	. . .	2.6 ± 0.4	22
SAF (Mojave)	14.3 ± 1.2	. . .	−2.7 ± 1.6	15
SAF (San Bernadino)	5.1 ± 1.5	. . .	1.0 ± 1.7	15
SAF (Salton Sea)	23.3 ± 0.5	. . .	1.5 ± 0.6	15
SAF (Imperial)	36.1 ± 0.7	. . .	−9.6 ± 0.5	0
SAF (Cerro Prieto)	40.0 ± 1.5	. . .	−6.5 ± 0.5	15
Eureka Peak	21.3 ± 1.6	. . .	−4.5 ± 1.0	5
Pinto Mountain	−9.4 ± 0.9	. . .	−9.2 ± 1.0	10
San Jacinto	11.9 ± 1.2	. . .	0.0 ± 0.7	10
Elsinore	2.7 ± 0.6	. . .	−0.6 ± 0.7	15
Rose Canyon	0.2 ± 2.5	. . .	0.8 ± 2.0	15
Oceanside	1.9 ± 3.2	. . .	2.6 ± 2.8	15
Coronado Bank	5.0 ± 3.0	. . .	−1.4 ± 1.9	15
San Clemente	3.1 ± 1.6	. . .	−1.9 ± 0.9	15
Hosgri	3.9 ± 0.6	. . .	0.7 ± 0.6	15
Agua Blanca	9.1 ± 2.7	. . .	0.7 ± 1.6	15
Newport – Inglewood	0.8 ± 1.6	. . .	0.3 ± 1.3	15
Palos Verdes	3.4 ± 1.4	. . .	3.1 ± 1.5	15
Raymond Hill	−2.3 ± 1.0	. . .	0.7 ± 1.7	15
Chino	0.1 ± 1.4	. . .	−4.0 ± 0.8	15
Puente Hills Thrust	−0.2 ± 1.1	4.2 ± 0.9	. . .	15
Cucamonga	−4.0 ± 1.3	10.0 ± 1.5	. . .	15
Hollywood Hills	−2.4 ± 1.1	−1.4 ± 2.3	. . .	15
Santa Monica Mountains	−2.4 ± 1.1	−0.2 ± 2.2	. . .	15
Sierra Madre (north)	3.1 ± 1.2	9.3 ± 2.4	. . .	15
Sierra Madre (south)	3.2 ± 1.5	3.9 ± 2.4	. . .	15
Santa Susana	3.1 ± 1.3	11.8 ± 2.5	. . .	15
San Cayetano	2.1 ± 1.3	4.2 ± 2.1	. . .	5
Oak Ridge	−8.5 ± 1.4	8.0 ± 2.2	. . .	5
White Wolf	1.3 ± 1.2	4.6 ± 1.7	. . .	15
North Frontal	−0.8 ± 1.7	3.0 ± 3.0	. . .	10
Coastal Ranges Split	5.5 ± 1.5	. . .	−2.3 ± 1.0	15
San Gabriel	3.8 ± 2.2	. . .	1.4 ± 2.0	15
Garlock (west)	−3.2 ± 1.5	. . .	4.7 ± 1.5	15
Garlock (central)	−1.8 ± 1.5	. . .	−0.2 ± 1.4	15
Garlock (east)	−1.1 ± 1.9	. . .	−5.2 ± 1.4	10
Blackwater-Landers	1.9 ± 0.6	. . .	0.1 ± 1.1	5
Helendale	2.2 ± 1.2	. . .	−2.1 ± 1.1	10
Goldstone	13.4 ± 1.0	. . .	0.0 ± 1.4	10
Eastern Mojave	−2.5 ± 0.8	. . .	−0.8 ± 0.8	10
Nevada Split	−0.9 ± 0.6	. . .	−2.6 ± 0.6	10
Airport Lake	7.3 ± 1.1	. . .	0.9 ± 1.5	10
Owens Valley	3.5 ± 0.9	. . .	−0.5 ± 0.8	10
Panamint Valley	3.1 ± 1.3	. . .	−3.3 ± 1.2	10
Death Valley	2.4 ± 1.2	. . .	−0.7 ± 0.9	10
Fish Lake	6.0 ± 2.1	. . .	−1.4 ± 1.0	10

[a] All rates are given in mm/yr. Positive and negative strike-slip rates give right- and left-lateral motion, respectively. Positive and negative dip-slip rates give thrust and normal motion, respectively. Positive and negative tensile-slip rates give closing and opening motion, respectively. In all cases, the slip rate is evaluated at the middle of the segment. SAF is an abbreviation for the San Andreas fault.

fault accommodates 4.6 ± 1.7 mm/yr of shortening. Through the Carrizo and Parkfield segments the SAF slips at ~36 mm/yr, in good agreement with Holocene estimates from offset stream channels [*Sieh and Jahns*, 1984].

7.6. Transverse Ranges and Los Angeles Basin

[39] The series of thrust faults that runs from the Cucamonga in the east, through the Sierra Madre, Santa Susana, San Cayetano, to the Oak Ridge in the west, accommodates between 3.0 and 11.8 mm/yr of dip-slip motion (Figure 13 and Table 2). The lowest slip rates are on the southern Sierra Madre fault. The highest slip rates are north of the Northridge rupture between the Big Pine and Oak Ridge blocks. Shortening rates vary along the San Gabriel Range front, decreasing southward along the Sierra Madre fault (9.3 ± 2.4–3.0 ± 2.4 mm/yr) then increasing along the Cucamonga fault (10.0 ± 1.5 mm/yr).

[40] We find between 0.5 and 8.0 mm/yr of shortening on both the northern and southern edges of the Ventura Basin. These rates are comparable to the convergence rates estimated by *Donnellan et al.* [1993a, 1993b] and *Hager et al.* [1999]. Convergence rates on the northern boundary decrease to the west, consistent with counterclockwise rotation relative to the Big Pine block. We are unable to constrain the seaward extent of the active Ventura Basin due to the lack of offshore geodetic observations. Counterclockwise rotation of the Oak Ridge block leads to a statistically insignificant amount of normal motion (0.2 ± 2.2 mm/yr) on the model Santa Monica Mountains fault. We find 2.3 ± 1.0 mm/yr of left-lateral motion on the Raymond Hill fault in, agreement with geologic estimates [*Weaver and Dolan*, 2000].

[41] Near the Los Angeles Basin, we find both right-lateral motion and shortening on the Newport-Inglewood (0.8 ± 1.6, 0.3 ± 1.3) and Palos Verdes faults (3.4 ± 1.4, 3.1 ± 1.5). In contrast to *Bawden et al.* [2001], our model suggests that shortening is more significant across the PHT (4.2 ± 0.9) than the Elysian Park Thrust (EPT). Residual velocities from models with an EPT structure replacing the PHT indicate the need for shortening west of the EPT. The residual velocities (Figure 11) show no indication of unmodeled deformation normal to the EPT. However, due to the fact that both faults are close together, it is difficult to distinguish rigorously between the two with available data. The PHT does not reach the surface in our model. Instead, the upper tip of the locked portion is buried at 3 km depth [*Shaw et al.*, 2002], consistent with creep on the up-dip extension of the PHT. This feature of our model significantly affects the interseismic velocity field; experiments with a range of burial depths have shown that this feature is required for the motion of the Los Angeles block to be consistent with left lateral faulting on the Raymond Hill fault. The shortening across the PHT is a consequence of the LA block impinging upon the BA block and moving away from the EL block. This also leads to opening along the Chino fault between the LA and EL blocks. With the Chino fault constrained to have only strike-slip motion, we still find 3.4 ± 0.9 mm/yr of dip-slip on the PHT. Thus our models provide evidence for the present day shortening across the PHT to complement geologic estimates of Holocene activity [e.g., *Dolan et al.*, 2003].

[42] To the south of the Los Angeles Basin, the counterclockwise rotation of the Palos Verdes block relative to the San Diego block leads to shortening across the Oceanside structure. Without block rotations, such a right-step in a right-lateral slipping fault system would be extensional, not compressional as we observe here.

7.7. Eastern California Shear Zone

[43] In the ECSZ, north of the Garlock fault (GF), our results are similar to those of *McClusky et al.* [2001]. The Owens Valley-Airport Lake fault system carries about 3.5–7.3 mm/yr of right-lateral motion, and the Panamint Valley-Hunter Mountain fault system, to the east, carries ~3 mm/yr. Our slip rate estimate for the Calico-Blackwater-Landers

structure (1.9 ± 0.6 mm/yr) is lower than *Peltzer et al.*'s [2001] estimate of 7 ± 3 mm/yr based on radar data. However, we find significant motion on the nearby Goldstone and Helendale faults (13.4 ± 1.0 and 2.2 ± 1.2 mm/yr respectively). This suggests that most of the deformation in the ECSZ is accommodated east of the Blackwater fault. GPS coverage in this area is exceedingly sparse and possibly influenced by postseismic deformation following the 1999 Hector Mine earthquake. In our model, we chose to recognize the limits of the data coverage and simplify the geometry in this region by using four north-south trending structures to accommodate all deformation.

[44] The southern end of the ECSZ is defined by the Pinto Mountain fault. Our model shows 9.4 ± 0.9 of left-lateral slip and 9.2 ± 1.0 mm/yr of opening along the central part of the fault, to the south-southeast of the Landers rupture. The opening rate is a result of the fast motion of the Goldstone fault to the north. It might be possible to decrease the amount of opening here by introducing a new connection from the ECSZ to the southern San Andreas fault along a structure such as the Hidden Springs fault.

8. Discussion

8.1. Slip Rates, Locking Depths, and Rheology Along the SAF and ECSZ

[45] For the Carrizo segment of the SAF (CSAF), we find that a 25 km locking depth fits the data best. The constraints on the CSAF locking depth are weak, in the sense that all locking depths from 15–40 km fit the data acceptably well (Figure 8). There are three obvious interpretations of a relatively deep locking depth. The first is that it represents the actual seismogenic depth. This is consistent the maximum depth of faulting estimated for the nearby Kern County earthquake [*Bawden*, 2001]. However, 25 km is deeper than the predicted depth of the brittle ductile transition (8–15 km) for a typical geotherm [e.g., *Kohlstedt et al.*, 1995] and below the maximum depth of seismicity directly beneath the CSAF [*Hauksson*, 2000]. A second explanation could be that the locking depth is actually shallower, but that variation in the elastic structure broadens the zone of strain accumulation [e.g., *Rybicki*, 1971; *Hager et al.*, 1999]. For this to be the case the shear modulus would have decrease with depth, the opposite of the behavior predicted by pressure effects and seismic observations.

[46] The third hypothesis is that a deep locking depth inferred using an elastic half-space model is indicative of viscoelastic deformation in the earth. Specifically, the broad zone of deformation late in a viscoelastic model of the earthquake cycle may be manifest as a deep locking depth in an elastic model [e.g., *Savage*, 1990; *Savage and Lisowski*, 1998]. As it has been approximately 150 years since the last Ft. Tejon SAF (FTSAF) earthquake, the CSAF would be in the latter half of its earthquake cycle if the mean recurrence interval were 200–300 years [*Sieh et al.*, 1989].

[47] *Savage and Lisowski* [1998] suggested that the Mojave SAF might be late in its earthquake cycle based on a deep locking depth estimated using trilateration data. They also assumed that the slip rate across the Mojave SAF was 34 mm/yr. We find that the slip rate of the Mojave segment of the SAF is at least 15 mm/yr slower and that there is no strong evidence for a deep locking depth. These two disparate results may be partially explained by noting that *Savage and Lisowski* [1998] only considered the SAF, and ignored the effects of deformation along the San Gabriel range front to the southwest**.** A second reason for these differences may be that *Savage and Lisowski* [1998] used data from an extremely narrow geodetic array, with only one station east of the SAF.

[48] However, we cannot rule out the possibility that the Mojave SAF may have a very poorly constrained and relatively deep locking depth. Models with a MSAF locking depth of 15 km and an imposed 30 mm/yr slip rate on the MSAF decrease the goodness of fit by 12%. Slip rate adjustments include a reduction in the estimated shortening rate along the Cucamonga fault to less than 2 mm/yr and left-lateral slip in excess of 7 mm/yr on the Sierra Madre fault as the San Gabriel block is squeezed out toward the Coast Ranges.

[49] While the estimated CSAF locking depth may be suggestive of long-term viscoelastic deformation, the success with which we have modeled the GPS velocities with an elastic model suggests that the low τ_0 (high viscosity) assumption may be more appropriate. In general, we do not see velocity gradients or locking depths that are consistent with high τ_0 (low viscosity) models. If $\tau_0 \approx 10(\eta = 2\text{–}3 \times 10^{18}$ Pa · s) then velocity gradients across a fault late in its earthquake cycle (e.g., southern SAF) would be very gradual (Figure 2), in contrast to the observed fault parallel velocities (Figure 5). Thus applying the *Savage and Prescott* [1978] periodic earthquake cycle model to interseismic deformation in southern California suggests that the viscosity of the lower crust/upper mantle is relatively high. If the mean recurrence time for the SAF is 200–300 years [*Sieh et al.*, 1989], then for $\tau_0 < 0.5$ (negligible variation through the seismic cycle) we would estimate that the viscosity of the lower crust/upper mantle is greater than $2\text{–}3 \times 10^{19}$ Pa · s.

[50] Recently, *Dixon et al.* [2003] presented a two-dimensional viscoelastic model for the ECSZ as a proposed explanation for the apparent disagreement between the geologic and geodetic slip rate estimates in Owens Valley. The high velocity gradient around the Owens Valley fault (Figures 4 and 5) is consistent with a fast slip rate from an elastic model. Our Owens Valley slip rate agrees with *McClusky et al.* [2001] within uncertainties, but it is higher than the 2 mm/yr Holocene estimate [*Beanland and Clark*, 1994]. *Dixon et al.* [2003] argued that the apparently fast slip rate on the Owens Valley fault could be due to postseismic relaxation following the 1872 Owens Valley earthquake. Their model also required that the Death Valley fault zone slips at a geologic rate of at least 8 mm/yr, and is currently very late in its earthquake cycle. Our block model shows that the high Owens Valley slip rate is not localized along the 1872 rupture zone. Instead, it extends along the entire Sierra Nevada range front. In order for postseismic relaxation to be responsible for this high slip rate, there would have to be three-dimensional postseismic relaxation phenomena that can cause velocity gradients to localize several fault lengths away from the coseismic rupture zone. This effect seems unlikely and a relatively fast Owens Valley slip rate is compatible with our three-dimensional block model (Figure 9) suggesting that the geodetic slip rate is fast compared with the Holocene estimate. An alternate

explanation is that the slip from earthquakes is hidden by distributed deformation in near surface sediments, thus limiting the amount of localized slip observable at the surface.

[51] Is it possible that the southern California velocity field looks like a steady state velocity field, not because of the absence of viscoelastic deformation, but because we are seeing the effects of averaging across rupture zones that are in different parts of the seismic cycles? This would be consistent with the observation that velocities from a viscoelastic seismic cycle model appear similar to steady state profiles approximately 40% of the way through a seismic cycle (Figure 2). However this seems unlikely, as major faults (SAF, SJF) that are likely to be late in their earthquake cycles show large localized velocity gradients (Figure 5). Thus, we cannot reject the steady state assumption we have invoked for our elastic block model. If viscoelastic relaxation through an earthquake cycle is important, it may be that only great earthquakes ($M_w > 8$) rupture to sufficient depths to generate a long-term postseismic response [e.g., *Savage and Prescott*, 1978].

8.2. Los Angeles Basin Tectonics

[52] The style of deformation in the Los Angeles Basin region has been debated over the past decade. *Walls et al.* [1998] argued for conjugate strike-slip faulting (escape tectonics), including left-lateral slip on the northern boundary of the Los Angeles Basin, based on the orientation of the principal strain rates derived from interseismic GPS measurements, but without accounting for elastic strain accumulation. *Argus et al.* [1999] used an a priori model for the SAF strain accumulation and found that the residual velocities suggested active shortening. This argument was refined by *Bawden et al.* [2001], who reached a similar conclusion using a comparable a priori strain accumulation model and a selected group of high quality GPS stations. Our model shows 4.2 ± 0.9 mm/yr of dip-slip on the PHT, in agreement with the active shortening inferred by both *Argus et al.* [1999] and *Bawden et al.* [2001]. However, we also find left-lateral slip along the Raymond Hill fault (2.3 ± 1.0 mm/yr) and right-lateral slip on the Newport-Inglewood fault (0.8 ± 1.6 mm/yr), consistent with some escape of material toward the Pacific Ocean, although not as much as suggested by *Walls et al.* [1998].

[53] Our slip rate model for the Los Angeles and Ventura basins differs from previous estimates for three reasons: data, geometry, and assumptions. First, we use a larger set of GPS velocities than any previous study of the Transverse Ranges. We also include aspects of the three-dimensional fault system geometry, such as the effects of multiple dipping and interacting fault zones. In addition, the blocks are allowed to rotate, introducing a component of motion absent from previous studies. Further, the block model uses both near and far-field velocities to estimate fault slip rates. Far field velocities (e.g., BA block) can constrain block motions and help to sort out the superposition of strain rates at complicated block boundaries. The third reason that our results differ from previous studies is that we do not make a priori assumptions about the slip rates of other faults in southern California. We estimate the slip rates on major active structures in the SCFS simultaneously. This allows us to find an internally consistent slip rate model where the same type of data has been used to estimate slip rates on all faults. In the Los Angeles Basin, the velocity gradients due to the elastic strain accumulation on the SAF and San Gabriel range front are comparable to the magnitude of the slip rates we are trying to estimate in the basin. Thus, with a large regional scale GPS data set, a three-dimensional model of the SCFS, and fewer a priori assumptions, we find evidence that both thickening and escape tectonics play an active role in the present day deformation of the LA basin.

8.3. Slip Rate Discrepancies Along the SAF, SJF, and ECSZ

[54] While many of our slip rate estimates agree with geologic estimates (e.g., CSAF, Raymond Hill), comparisons between geodetic and geologic slip rates along the SBSAF, SJF and ECSZ show large discrepancies. We argue that a model that allows for the effects of rapid evolution of the SCFS may reconcile these discrepancies. Following the 1992 Landers earthquake, *Nur et al.* [1993a, 1993b] suggested that the Mojave Desert might be currently undergoing reorganization. Slip rate discrepancies along the Owens Valley, San Andreas and San Jacinto faults suggest that this behavior is not localized in the Mojave Desert.

[55] Like *Peltzer et al.* [2001], we find that the Blackwater fault slip rate is fast relative to *Oskin and Irondio*'s [2004] submillimeter per year geologic estimate based on the offset of Pliocene lava flows. Geodetic slip rates inferred along the southern extension of this structure are also fast relative to estimates of Holocene activity [*Rockwell et al.*, 2000]. It is difficult to argue that postseismic deformation following the 1992 Landers and/or 1999 Hector Mine earthquakes is entirely responsible for the relatively fast slip rates in the Mojave, because *Sauber et al.* [1994] estimated similar deformation rates prior to the event. Similarly, we find that our Owens Valley slip rate is approximately twice as fast as the 2 mm/yr Holocene estimate [*Beanland and Clark*, 1994]. East of the Blackwater and Airport Lake faults, we find that the Garlock fault moves left-laterally at 1.1 ± 1.9 mm/yr. Part of this segment cuts past Searles Lake, where *McGill and Sieh* [1993] estimated a slip rate of 7 ± 2 mm/yr over the last 60,000 years. Our model, like that of *Peltzer et al.* [2001], suggests that the Blackwater and Owens valleys are more active than they have been in the recent past, while the Garlock is now less active.

[56] We find a similar discrepancy for the SJF. *Sharp* [1981] reported that geomorphic evidence suggested that the SJF had accelerated in the late Holocene (from 2–5 mm/yr) as well as a 12 mm/yr mean slip rate through the latter half of the Quaternary. We find that the geodetic rate (11.9 ± 1.2 mm/yr) agrees well with *Sharp*'s [1981] 12 mm/yr late Quaternary average but is much faster than the late Holocene estimate, suggesting that the SJF has been less active in the recent past.

[57] The relatively slow slip rate estimate on the San Bernadino segment of the SAF (SBSAF, 5.1 ± 1.5 mm/yr, Figure 12) is one of the more interesting block model results. *Bird and Rosenstock* [1984] and *Bird and Kong* [1994] found low rates, though they preferred a higher upper bound. *Potter* [1997] also suggested that geologic slip rate estimates were too high to accurately model the geodetic data in this region and *Becker et al.* [2005]

estimated a 2.3 ± 15.0 mm/yr right-lateral strike-slip rate on the SBSAF using geodetic and focal mechanism data. Our low slip rate estimate differs substantially from the 14,000-year geologic average of 25 ± 4 mm/yr [*Weldon and Sieh*, 1985]. There are four obvious possible explanations for this apparent disagreement. The first and second are that either the block model or the geologic slip rate estimates are wrong. By testing the block model with an a priori 25 mm/yr slip rate imposed on the San Bernadino segment, we can demonstrate that a high slip rate is not compatible with the geodetic data (Figure 14). The residual velocities are larger and the overall and local misfit criteria increase by 18% and 62%, respectively. Further, the correlation between residual velocity magnitude and the elastic deformation increases by 42%, indicating a systematic increase in the magnitude of near-fault residual velocities. The slow SBSAF strike slip rate is not dependant on the existence of the small San Bernadino block (Figure 6). Models without the SB block (western North Frontal fault removed) yield a 2.7 ± 1.1 mm/yr SBSAF slip rate. The proximity of this area to the location of the 1992 Landers earthquake raises the question of whether the GPS data in this area may not be representative of steady interseismic velocities. For this to be the effect controlling the slip rate estimates, the rapid postseismic decay would have to extend across the Mojave and Salton blocks, more than 150 km from the rupture zone. The possibility of local seismic cycle variations causing this result seems remote, as locking depths as deep as 300 km increase the SBSAF slip rate by no more than 3 mm/yr. *Smith and Sandwell* [2003] used the SCECCMM3.0 velocities and an interseismic strain accumulation model for the SAF to estimate a 22.6 km locking depth on the SBSAF with an assumed slip rate of 28 mm/yr. *Weldon and Sieh*'s [1985] slip rate estimate is robust, which leads us to the arguments for the compatibility of the geologic and geodetic slip rate estimates.

[58] The most obvious way in which the two rates could be compatible is if they are in different places. *Weldon and Sieh*'s [1985] study area is near Cajon Creek. We have chosen not to elongate the northern part of the Salton block into a small sliver that runs between the Mojave Desert and the San Gabriel Mountains (Figures 6 and 14) [*Jennings*, 1994]. If the San Jacinto fault reconnects with the SAF to the south of Cajon Creek, then our slip rate estimate is closer to Weldon and Sieh's, but would apply to the Mojave SAF, not the SBSAF. However this would not eliminate the low slip rate segment between the northern intersection of the SJF and SAF and the westernmost connection between the ECSZ and the SAF through the Eureka Peak fault.

[59] The incompatibility between geologic and geodetic estimates may be reconciled if fault behavior is changing rapidly. This would require that the apparent SBSAF rate has evolved over the later half of the Holocene. It could be the case that our SBSAF slip rate estimate appears substantially slower than the *Weldon and Sieh* [1985] rate because the effects of temporally clustered earthquakes are important. A clustered earthquake cycle consists of an active period, with a number of large earthquakes on the same fault, followed by a less active quiescent period. If the geologic observations of activity on the SBSAF include the effects of an active period that occurred between 4000 and 14,000 years ago, the apparent geologic slip rate may appear to be substantially faster than the long-term average. Conversely, if geologic observations are focused on a quiescent period, then a slip rate estimate based on geodetic observations may appear faster than a geologic estimate.

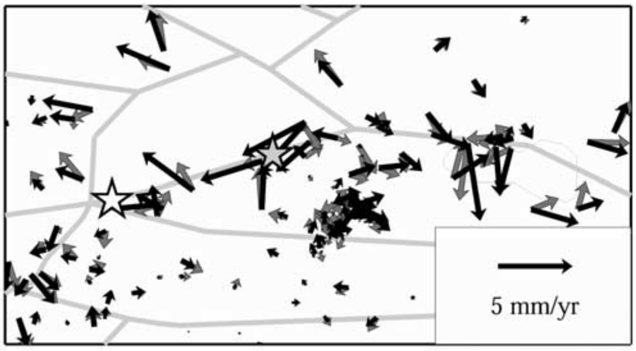

Figure 14. Residual velocities and fault system geometry along the San Bernadino segment of the San Andreas fault (SBSAF). The gray arrows are the residuals for our preferred model where there are no constraints on the SBSAF and the estimated right lateral slip rate is 5.1 ± 0.9 mm/yr. The black arrows are the residuals when the SBSAF is forced to slip at 25 mm/yr. The white and gray stars are the study areas from *Weldon and Sieh* [1985] and *Yule and Sieh* [2000].

[60] If the both the SJF and ECSZ have been relatively quiescent through the Holocene we would expect the geodetic rates to be faster than geologic rates. Conversely, if the SBSAF has been relatively active through the last 14,000 years, the geologic rates could be greater than the geodetic rates. The slip rates estimated from our block model are consistent with both of these expectations. In a viscoelastic model, earthquake clustering can lead to velocity profiles that are similar to steady state profiles even at long times after the most recent rupture [*Meade and Hager*, 2004]. Interestingly, the apparent deceleration of the SBSAF is nearly balanced by the acceleration of the SJF and ECSZ. This implies that the slip budget across the SCFS might appear constant even in the presence of clustered earthquake activity. Future paleoseismic studies could provide the rupture history observations necessary to resolve these apparent slip rate discrepancies.

[61] If the SBSAF is moving ∼5 mm/yr, there are direct implications for seismic hazard potential. The slower a fault slips, the longer it will take to accumulate a given amount of elastic strain in the bounding blocks. If earthquakes occur quasi-periodically, this would imply a longer recurrence interval for a given magnitude earthquake. *Yule and Sieh* [2000] reported preliminary results suggesting ∼330 year recurrence intervals for this segment of the SAF. A slow slip rate may also act as a kinematic barrier to rupture propagation as this segment of the SAF may rupture less frequently than adjacent segments. This provides a possible explanation for the southern termination of the 1857 rupture, which stopped just to the north of this segment [*Sieh*, 1978].

9. Conclusions

[62] Fault slip rates can be estimated using a block model that accounts for the effects of steady state elastic strain

accumulation and block rotations on a sphere. Block motions and fault slip rates are constrained by GPS observations of interseismic deformation and the three-dimensional geometry of the fault system. We have used this model to estimate fault slip rates across the southern California fault system.

[63] Estimated strike-slip rates on the San Andreas fault vary by at least a factor of five, from ~36 mm/yr along the Carrizo segment to ~5 mm/yr along the San Bernadino segment. The San Bernadino San Andreas fault slip rate is relatively slow due to the relative motion between the Salton and San Bernadino/Mojave blocks and may serve as a kinematic barrier to the rupture of earthquakes from the central to southern SAF.

[64] Slip rates in and around the Los Angeles Basin are consistent with both thickening and escape tectonics. Dip-slip motion on the Puente Hills Thrust and Sierra Madre fault accommodates active shortening, while left-lateral motion along the southern San Gabriel range front and Raymond Hill fault allows for the escape of material from the Big Bend of the San Andreas fault.

[65] The lack of observable long-term postseismic deformation effects leads us to infer that the viscosity of the lower crust/upper mantle is relatively high. An alternate explanation is that the viscosity of the lower crust/upper mantle is relatively low, but due to the effects from different rupture zones in different parts of the earthquake cycle, we see a superposition of velocities that appears similar to a steady state velocity field. However, this seems improbable due to the observation of localized velocity gradients around faults that are likely late in their earthquake cycles (e.g., San Andreas fault).

[66] Systematic differences between geologic and geodetic slip rates can be explained by time dependent behavior of the southern California fault system. The San Bernadino San Andreas fault appears less active relative to Holocene estimates. In contrast, the San Jacinto fault and faults in the Eastern California Shear Zone are relatively more active compared with geologic estimates, possibly due the effects of temporally clustered earthquakes. The block modeling approach provides a framework for combining geologic and geodetic fault slip rate estimates to better understand the relationship between short- and long-term fault system behaviors.

[67] **Acknowledgments.** This research was supported by the southern California Earthquake Center. SCEC is funded by NSF Cooperative Agreement EAR-0106924 and USGS Cooperative Agreement 02HQAG0008. The SCEC contribution number for this paper is 816. Figures 1, 4, 6, 9, 11, 12, 13, and 14, were generated with the help of the Generic Mapping Tools [*Wessel and Smith*, 1991]. We thank Robert King, Thomas Herring and Duncan Agnew for helpful discussions regarding the SCEC CMM 3.0. Simon McClusky generously provided us with updated GPS velocities in the Eastern California shear zone. John Shaw and Andreas Plesch provided useful suggestions regarding the geometry of the southern California fault system. Donald Argus, David Sandwell, and an anonymous associate editor provided thoughtful reviews.

References

Argus, D. F., and R. G. Gordon (2001), Present tectonic motion across the Coast Ranges and San Andreas fault system in central California, *Geol. Soc. Am. Bull.*, *113*, 1580–1592.

Argus, D. F., M. B. Helfin, A. Donnellan, F. H. Webb, D. Dong, K. J. Hurst, D. C. Jefferson, G. A. Lyzenga, M. M. Watkins, and J. F. Zumberge (1999), Shortening and thickening of metropolitan Los Angeles measured and inferred using geodesy, *Geology*, *27*, 703–706.

Bawden, G. W. (2001), Source parameters for the 1952 Kern County earthquake, California: A joint inversion of leveling and triangulation observations, *J. Geophys. Res.*, *106*, 771–786.

Bawden, G. W., W. Thatcher, R. Stein, K. W. Hudnut, and G. Peltzer (2001), Tectonic contraction across Los Angeles after removal of groundwater pumping effects, *Nature*, *412*, 812–815.

Beanland, S., and M. M. Clark (1994), The Owens Valley fault zone, eastern California, and surface faulting associated with the 1872 earthquake, *U.S. Geol. Surv. Bull.*, *1982*, 1–29.

Becker, T. W., J. L. Hardebeck, and G. Anderson (2005), Constraints on fault slip rate of the southern California plate boundary from GPS velocity and stress inversions, *Geophys. J. Int.*, in press.

Bennett, R. A., W. Rodi, and R. E. Reilinger (1996), Global Positioning System constraints on fault slip rates in southern California and northern Baja, Mexico, *J. Geophys. Res.*, *101*, 21,943–21,960.

Bennett, R. A., B. P. Wernicke, J. L. Davis, P. Elosegui, J. K. Snow, M. J. Abolins, M. A. House, G. L. Stirewalt, and D. A. Ferrill (1997), Global Positioning System constraints on fault slip rates in the Death Valley region, California and Nevada, *Geophys. Res. Lett.*, *24*, 3073–3076.

Bird, P., and X. Kong (1994), Computer simulations of California tectonics confirm very slow strength of major faults, *Geol. Soc. Am. Bull.*, *106*, 159–174.

Bird, P., and R. W. Rosenstock (1984), Kinematics of present crust and mantle flow in southern California, *Geol. Soc. Am. Bull.*, *95*, 946–957.

Cheng, A., D. D. Jackson, and M. Matsu'ura (1987), Aseismic crustal deformation in the Transverse Ranges of southern California, *Tectonophysics*, *144*, 159–180.

DeMets, C., and T. Dixon (1999), New kinematic models for Pacific-North America motion from 3 Ma to present: 1. Evidence for steady motion and biases in the NUVEL-1A model, *Geophys. Res. Lett.*, *26*, 1921–1924.

DeMets, C., R. G. Gordon, D. F. Argus, and S. Stein (1990), Current plate motions, *Geophys. J. Int.*, *101*, 425–478.

Dixon, T. H., M. Miller, F. Farina, H. Wang, and D. Johnson (2000), Present-day motion of the Sierra Nevada block and some tectonic implications for the Basin and Range province, North American Cordillera, *Tectonics*, *19*, 1–24.

Dixon, T. H., E. Norabuena, and L. Hotaling (2003), Paleoseismology and Global Positioning System: Earthquake-cycle effects and geodetic versus geologic fault slip rates in the Eastern California Shear Zone, *Geology*, *31*, 55–58.

Dolan, J. F., S. A. Christofferson, and J. H. Shaw (2003), Recognition of paleoearthquakes on the Puente Hills blind thrust fault, California, *Science*, *300*, 115–118.

Donnellan, A., B. H. Hager, and R. W. King (1993a), Discrepancy between geological and geodetic deformation rates in the Ventura Basin, *Nature*, *366*, 333–336.

Donnellan, A., B. H. Hager, R. W. King, and T. A. Herring (1993b), Geodetic measurement of deformation in the Ventura Basin region, southern California, *J. Geophys. Res.*, *98*, 21,727–21,739.

Ellsworth, W. L. (1990), Earthquake history, 1769–1989, in *The San Andreas Fault System, California*, edited by R. E. Wallace, *U.S. Geol. Surv. Prof. Pap.*, *P 1515*, 153–187.

Feigl, K. L., R. W. King, and T. H. Jordan (1990), Geodetic measurement of tectonic deformation in the Santa Maria fold and thrust belt, California, *J. Geophys. Res.*, *95*, 2679–2699.

Feigl, K. L., et al. (1993), Space geodetic measurement of crustal deformation in central and southern California, *J. Geophys. Res.*, *98*, 21,677–21,712.

Gan, W., J. L. Svarc, J. C. Savage, and W. H. Prescott (2000), Strain accumulation across the Eastern California Shear Zone at latitude 36°30′N, *J. Geophys. Res.*, *105*, 16,229–16,236.

Hager, B. H., G. A. Lyzenga, A. Donnellan, and D. Dong (1999), Reconciling rapid strain accumulation with deep seismogenic fault planes in the Ventura Basin, California, *J. Geophys. Res.*, *104*, 25,207–25,219.

Hanks, T. C., and H. Kanamori (1979), A moment magnitude scale, *J. Geophys. Res.*, *84*, 2348–2350.

Hauksson, E. (2000), Crustal structure and seismicity distribution adjacent to the Pacific and North America plate boundary in southern California, *J. Geophys. Res.*, *105*, 13,875–13,903.

Hearn, E. H., and E. D. Humphreys (1998), Kinematics of the southern Walker Lane Belt and motion of the Sierra Nevada block, California, *J. Geophys. Res.*, *103*, 27,033–27,049.

Hubert-Ferrari, A., A. Barka, E. Jacques, S. Nalbant, B. Meyer, R. Armijo, P. Tapponier, and G. King (2000), Seismic hazard in the Marmara Sea region following the 17 August 1999 Izmit earthquake, *Nature*, *404*, 269–271.

Hudnut, K. W., et al. (1994), Co-seismic displacements of the 1992 Landers earthquake sequence, *Bull. Seismol. Soc. Am.*, *84*, 625–645.

Hudnut, K. W., et al. (1996), Co-seismic displacements of the 1994 Northridge, California, earthquake, *Bull. Seismol. Soc. Am.*, *86*, 19–36.

Jennings, C. W. (1994), Fault activity map of California and adjacent areas with location and ages of recent volcanic eruptions, *Calif. Geol. Data Map Ser., Map 6*, Calif. Dept. of Conserv., Div. of Mines and Geol., Sacramento, Calif.

Johnson, H. O., D. C. Agnew, and F. K. Wyatt (1994), Present-day crustal deformation in southern California, *J. Geophys. Res.*, *99*, 23,951–23,974.

Kaverina, A., D. Dreger, and E. J. Price (2002), The combined inversion of seismic and geodetic data for the source process of the 16 October 1999 M_w 7.1 Hector Mine, California, earthquake, *Bull. Seismol. Soc. Am.*, *92*, 1266–1280.

Kohlstedt, D. L., B. Evans, and S. J. Mackwell (1995), Strength of the lithosphere: Constraints imposed by laboratory experiments, *J. Geophys. Res.*, *100*, 17,587–17,602.

Lyons, S. N., and D. Sandwell (2003), Fault creep along the southern San Andreas from interferometric synthetic aperture radar, permanent scatterers, and stacking, *J. Geophys. Res.*, *108*(B1), 2047, doi:10.1029/2002JB001831.

Malvern, L. E. (1969), Introduction to the mechanics of a continuous medium, 713 pp., Prentice Hall, Upper Saddle River, N. J.

Matsu'ura, M., and D. D. Jackson (1986), Dislocation model for aseismic crustal deformation at Hollister, California, *J. Geophys. Res.*, *91*, 12,661–12,674.

McCaffrey, R. (1996), Estimates of modern arc-parallel strain rates in fore arcs, *Geology*, *24*, 27–30.

McClusky, S. C., S. C. Bjornstad, B. H. Hager, R. W. King, B. J. Meade, M. M. Miller, F. C. Monastero, and B. J. Souter (2001), Present day kinematics of the Eastern California Shear Zone from a geodetically constrained block model, *Geophys. Res. Lett.*, *28*, 3339–3372.

McGill, S., and T. Rockwell (1998), Ages of late Holocene earthquakes on the central Garlock fault near El Paso Peaks, California, *J. Geophys. Res.*, *103*, 7265–7279.

McGill, S., and K. Sieh (1993), Holocene slip rate of the central Garlock fault in southeastern Searles Valley, California, *J. Geophys. Res.*, *98*, 14,217–14,231.

Meade, B. J., and B. H. Hager (2001), The current distribution of deformation in the Western Tien Shan from block models constrained by geodetic data, *Geol. Geof.*, *42*, 1622–1633.

Meade, B. J., and B. H. Hager (2004), Viscoelastic deformation for a clustered earthquake cycle, *Geophys. Res. Lett.*, *31*, L10610, doi:10.1029/2004GL019643.

Meade, B. J., B. H. Hager, S. C. McClusky, R. E. Reilinger, S. Ergintav, O. Lenk, A. Barka, and H. Ozener (2002), Estimates of seismic potential in the Marmara Sea region from block models of secular deformation constrained by Global Positioning System measurements, *Bull. Seismol. Soc. Am.*, *92*, 208–215.

Miller, M. M., D. J. Johnson, T. H. Dixon, and R. K. Dokka (2001), Refined kinematics of the Eastern California Shear Zone from GPS observations, 1993–1998, *J. Geophys. Res.*, *106*, 2245–2263.

Minster, B., and T. H. Jordan (1987), Vector constraints on western U.S. deformation from space geodesy, neotectonics, and plate motions, *J. Geophys. Res.*, *92*, 4798–4804.

Murray, M. H., and P. Segall (2001), Modeling broad scale deformation in northern California and Nevada from plate motions and elastic strain accumulation, *Geophys. Res. Lett.*, *28*, 4315–4318.

Murray, J. R., P. Segall, P. Cervelli, W. Prescott, and J. Svarc (2001), Inversion of GPS data for spatially variable slip-rate on the San Andreas fault near Parkfield, CA, *Geophys. Res. Lett*, *28*, 359–362.

Nur, A., and G. Mavko (1974), Postseismic viscoelastic rebound, *Science*, *183*, 204–206.

Nur, A., H. Ron, and G. Beroza (1993a), Landers-Mojave earthquake line: A new fault system?, *GSA Today*, *3*, 253, 256–258.

Nur, A., H. Ron, and G. C. Beroza (1993b), The nature of the Landers-Mojave earthquake line, *Science*, *261*, 201–203.

Okada, Y. (1985), Surface deformation due to shear and tensile faults in a half space, *Bull. Seismol. Soc. Am.*, *75*, 1135–1154.

Oskin, M., and A. Iriondo (2004), Large magnitude transient strain accumulation on the Blackwater fault, Eastern California Shear Zone, *Geology*, *32*, 313–316.

Peltzer, G., F. Crampe, S. Hensley, and P. Rosen (2001), Transient strain accumulation and fault interaction in the Eastern California Shear Zone, *Geology*, *29*, 975–978.

Petersen, M. D., and S. G. Wesnousky (1994), Fault slip rates and earthquake histories for active faults in southern California, *Bull. Seismol. Soc. Am.*, *84*, 1608–1649.

Pollitz, F. F., G. Peltzer, and R. Burgmann (2000), Mobility of continental mantle: Evidence from postseismic geodetic observations following the 1992 Landers earthquake, *J. Geophys. Res.*, *105*, 8035–8054.

Potter, D. R. (1997), Long-term postseismic relaxation in southern California: Evidence from a geostatistical analysis of geodetic data, Ph.D. dissertation, Univ. of Calif., Los Angeles.

Rockwell, T. K., S. Lindvall, M. Herzberg, D. Murback, T. Dawson, and G. Berger (2000), Paleoseismology of the Johnson Valley, Kickapoo, and Homestead Valley faults: Clustering of earthquakes in the Eastern California Shear Zone, *Bull. Seismol. Soc. Am.*, *90*, 1200–1236.

Rybicki, K. (1971), The elastic residual field of a very long strike-slip fault in the presence of a discontinuity, *Bull. Seismol. Soc. Am.*, *61*, 79–92.

Sauber, J., W. Thatcher, and S. C. Solomon (1986), Geodetic measurement of deformation in the central Mojave Desert, California, *J. Geophys. Res.*, *91*, 12,683–12,693.

Sauber, J., W. Thatcher, S. C. Solomon, and M. Lisowski (1994), Geodetic slip rate for the Eastern California Shear Zone and the recurrence time of Mojave Desert earthquakes, *Nature*, *367*, 264–266.

Saucier, F., and E. Humphreys (1993), Horizontal crustal deformation in southern California from joint models of geologic and very long baseline interferometry measurements, in *Contributions of Space Geodesy to Geodynamics: Crustal Dynamics*, *Geodyn. Ser.*, vol. 23, edited by D. E. Smith and D. L. Turcotte, pp. 139–176, AGU, Washington, D. C.

Savage, J. C. (1990), Equivalent strike-slip earthquakes cycles in half-space and lithosphere-athenosphere Earth models, *J. Geophys. Res*, *95*, 4873–4879.

Savage, J. C. (2000), Viscoelastic coupling model for the earthquake cycle driven from below, *J. Geophys. Res.*, *105*, 25,525–25,532.

Savage, J. C., and R. O. Burford (1973), Geodetic determination of the relative plate motion in central California, *J. Geophys. Res.*, *78*, 832–845.

Savage, J. C., and M. Lisowski (1998), Viscoelastic coupling model of the San Andreas fault along the Big Bend, southern California, *J. Geophys. Res.*, *103*, 7281–7292.

Savage, J. C., and W. H. Prescott (1978), Asthenosphere readjustment and the earthquake cycle, *J. Geophys. Res.*, *83*, 3369–3376.

Savage, J. C., M. Lisowski, and W. H. Prescott (1990), An apparent shear zone trending north-northwest across the Mojave Desert into Owens Valley, eastern California, *Geophys. Res. Lett.*, *17*, 2113–2116.

Savage, J. C., W. Gan, and J. L. Svarc (2001), Strain accumulation and rotation in the Eastern California Shear Zone, *J. Geophys. Res.*, *106*, 21,995–22,007.

Segall, P. (2002), Integrating geologic and geodetic estimates of slip rate on the San Andreas fault system, *Int. Geol. Rev.*, *44*, 62–82.

Sella, G. F., T. H. Dixon, and A. Mao (2002), REVEL: A model for recent plate velocities from space geodesy, *J. Geophys. Res.*, *107*(B4), 2081, doi:10.1029/2000JB000033.

Sharp, R. V. (1981), Variable rates of late Quaternary strike slip on the San Jacinto fault zone, southern California, *J. Geophys. Res.*, *86*, 1754–1762.

Shaw, J. H., A. Plesch, J. F. Dolan, T. L. Pratt, and P. Fiore (2002), Puente Hills blind-thrust system, Los Angeles, California, *Bull. Seismol. Soc. Am.*, *92*, 2946–2960.

Sieh, K. (1978), Slip along the San Andreas fault associated with the great 1857 earthquake, *Bull. Seismol. Soc. Am.*, *68*, 1421–1428.

Sieh, K. E., and R. H. Jahns (1984), Holocene activity of the San Andreas fault at Wallace Creek, California, *Geol. Soc. Am. Bull.*, *95*, 883–896.

Sieh, K., M. Stuiver, and D. Brillinger (1989), A more precise chronology of earthquakes produced by the San Andreas fault in southern California, *J. Geophys. Res.*, *94*, 603–623.

Shen, Z.-K., D. D. Jackson, and B. X. Ge (1996), Crustal deformation across and beyond the Los Angeles Basin from geodetic measurements, *J. Geophys. Res.*, *101*, 27,957–27,980.

Smith, B., and D. Sandwell (2003), Coulomb stress accumulation along the San Andreas Fault system, *J. Geophys. Res.*, *108*(B6), 2296, doi:10.1029/2002JB002136.

Souter, B. J. (1998), Comparisons of geological models to GPS observations in southern California, Ph.D. dissertation, Mass. Inst. of Technol., Cambridge.

Steblov, G. M., M. G. Kogan, R. W. King, C. H. Scholz, R. Bürgmann, and D. I. Frolov (2003), Imprint of the North American plate in Siberia revealed by GPS, *Geophys. Res. Lett.*, *30*(18), 1924, doi:10.1029/2003GL017805.

Stein, R. S., and T. C. Hanks (1998), $M \geq 6$ earthquakes in southern California during the twentieth century: No evidence for a seismicity or moment deficit, *Bull. Seismol. Soc. Am.*, *88*, 635–652.

Walls, C., T. Rockwell, K. Mueller, Y. Bock, S. Williams, J. Pfanner, J. Dolan, and P. Feng (1998), Escape tectonics in the Los Angeles metropolitan region and implications for seismic risk, *Nature*, *394*, 356–360.

Ward, S. N. (1998), On the consistency of earthquake moment rates, geologic fault data, and space geodetic strain: The United States, *Geophys. J. Int.*, *134*, 172–186.

Wdowinski, S., Y. Sudman, and Y. Bock (2001), Geodetic detection of active faults in S. California, *Geophys. Res. Lett*, *28*, 2321–2324.

Weaver, K. D., and J. F. Dolan (2000), Paleoseismology and geomorphology of the Raymond fault, Los Angeles County, California, *Bull. Seismol. Soc. Am.*, *90*, 1409–1429.

Weldon, R. J., and E. D. Humphreys (1986), A kinematic model of southern California, *Tectonics*, *5*, 33–48.

Weldon, R. J., and K. E. Sieh (1985), Holocene rate of slip and tentative recurrence interval for large earthquakes on the San Andreas fault, Cajon Pass, southern California, *Geol. Soc. Am. Bull.*, *96*, 793–812.

Wessel, P., and W. H. F. Smith (1991), Free software helps map and display data, *Eos Trans. AGU*, *72*, 441, 445–446.

Yule, D., and K. Sieh (2000), The paleoseismic record at Burro Flats; evidence for a 300-year average recurrence for large earthquakes on the San Andreas fault in San Gorgonio Pass, southern California, *Geol. Soc. Am. Abstr. Programs*, *33*, 31.

B. Hager, Department of Earth, Atmospheric and Planetary Sciences, Massachusetts Institute of Technology, 77 Massachusetts Avenue, Cambridge, MA 02139, USA.

B. J. Meade, Department of Earth and Planetary Sciences, Harvard University, 20 Oxford Street, Cambridge, MA 02138, USA. (meade@rupture.harvard.edu)